THERMAL MODELING OF AIR COOLED OUTDOOR DIGITAL DISPLAYS

A Dissertation
Presented to
The Academic Faculty

by

Jeho Kim

In Partial Fulfillment
of the Requirements for the Degree
Master's in the
Science in Mechanical Engineering

Georgia Institute of Technology
December 2019

THERMAL MODELING OF
AIR COOLED OUTDOOR DIGITAL DISPLAYS

Approved by:

Dr. Yogendra Joshi, Advisor
School of Mechanical Engineering
Georgia Institute of Technology

Dr. Zhuomin Zhang
School of Mechanical Engineering
Georgia Institute of Technology

Dr. Mostafa Ghiaasiaan
School of Mechanical Engineering
Georgia Institute of Technology

Date Approved: October 17, 2019

To my parents

Seokman Kim and Miok Yoon

&

To my younger brother

Jehong Kim

ACKNOWLEDGEMENTS

I would like to thank J. Michael Brown and Dr. Yogendra Joshi for giving me this wonderful opportunity to be a part of a collaborative research between Manufacturing Resources International and Georgia Institute of Technology. I couldn't have pursed a degree in Master of Science in Mechanical Engineering if it weren't for their support. I would also like to thank Kevin O'Connor, Marcos Diaz, Dr. Zhuomin Zhang, Dr. Mostafa Ghiaasiaan and Peiyan Yang for their valuable feedback on my work, along with the remaining crew of MRI for their assistance. Last but not least, I would like to thank my parents and brother who have supported me since the day we moved to the United States.

TABLE OF CONTENTS

LIST OF TABLES

LIST OF FIGURES

LIST OF SYMBOLS AND ABBREVIATIONS

Symbols

A	surface area, m^2
E	electric field, V/m
G	solar irradiance, W/m^2
I	intensity, W/m^2
I_λ	spectral intensity, W/m^3
$I_{\lambda,a}$	absorbed spectral intensity, W/m^3
$I_{\lambda,i}$	spectral solar intensity, W/m^3
$I_{b\lambda}$	spectral blackbody intensity, W/m^3
Q	heat load, W
K	system curve constant, $Pa/(m^3/s)^2$
S	poynting vector, W/m^2
a_λ	spectral absorption coefficient, 1/m
c	phase speed, m/s
q	volumetric flow rate, m^3/s
t	thickness, m
BLU	backlight unit
CCFL	cold cathode fluorescent lamp
CFD	computational fluid dynamics
FTIR	fourier transform infrared spectrometer
HT	heat transfer
LCD	liquid crystal display

LED	light emitting diode
MRI	manufacturing resources international
n	refractive index

Greek Letters

λ	wavelength, m
μ_0	permeability, N/A^2
σ_s	scattering coefficient, 1/m
α_λ	spectral absorptance
η	absorption factor
κ	extinction coefficient
τ_λ	spectral transmittance
Φ	phase function

SUMMARY

The thermal design process for many electronic products often minimizes the use of computational fluid dynamics and heat transfer (CFD/HT) software in favor of quick prototyping and testing to determine the thermal characteristics of the product. For large-scale products with many thermal challenges, such a strategy may be impractical due to the high cost of prototyping, time constraints and inevitable iterations involved. In such cases, carefully developed and validated simulation models are very valuable in driving the product design. Based on this idea, a methodology for thermal design of outdoor digital displays is described in this study.

Both the surrounding ambient temperature and solar irradiance are major contributors to air temperature rise within such displays, but most CFD/HT software packages are limited in simulating solar irradiance through semi-transparent materials and multiple surfaces. Therefore, the contribution from solar irradiance must be treated with care when creating CFD/HT models, especially when an optimum number of mesh elements is to be used to minimize the necessary processing power and solution computation time. To best accommodate the effect of solar irradiance, in lieu of defining the solar irradiance as a heat flux, a methodology to assign the power that should be imposed on the sun-exposed display components is described.

Simulation results are obtained for a range of environmental temperature and irradiance values and are compared with experimental data. The simulation study examines a variation in simulation results which is sensitive to mesh element numbers,

meshing techniques and simulation packages. It is shown that CFD/HT software can be used effectively as a means of making conservative design choices.

The liquid crystal display (LCD), optical films, and diffuser experience a deflection due to the body force and pressure difference inside the outdoor digital display. As the dimension of the air gap located between the vandal glass and diffuser changes according to the deflection, a change in maximum temperature of the LCD, and fan performance due to the gap change are predicted. The gap modification is applied uniformly throughout the diffuser and does not best reflect how the bending takes place in reality, yet such parametric study could also assist in determining the optimum gap that promises the best thermal performance in the LCD if the pressure difference is low and the diffuser stays relatively flat. It is concluded that the internal fans experience less pressure drop as the gap increases, and the LCD does not suffer a significant temperature rise as long as the gap remains within 7 mm to 9 mm range.

CHAPTER 1. INTRODUCTION

As LCD technology advances to larger sizes and higher resolution, many companies are exploring their use of outdoor signage as a replacement for traditional poster advertising. The majority of LCDs are meant to be used indoors with little to no exposure to the open environment, such as the consumer television or the computer monitor. Yet, due to a higher demand for outdoor uses, such digital displays have become increasingly popular and more common in streets, bus stops, and other public facilities [1]. While the outdoor digital displays, as shown in Figure 1, offer more versatility in terms of their deployment sites, they face unique thermal challenges that are not present in the indoor displays which include:

1. Exposure to high ambient temperature
2. Direct solar irradiation
3. Higher power consumption necessary for achieving sunlight readability
4. Corrosion in sensitive display components due to moisture, dust and pollution in the ambient air.

Thus, it is crucial to check the sustainability of the displays under a thermally challenging outdoor condition defined by the above constraints. The research focuses on a development of reliable thermal models of the outdoor digital displays which can be used to predict the maximum temperature of display components under the worst ambient air temperature and solar irradiance. For the ambient air, at the time of summer, the midday temperature in middle hemisphere typically hits in between 43 °C to 46 °C [2]. It is known that about 1,000 W/m^2 of the solar irradiance reaches the ground at sea level in

Figure 1 – 55” outdoor digital display deployed in Georgia Institute of Technology

which the amount increases as the altitude increases and reaches up to 1,300 W/m^2 at the top of the atmosphere [3]. In this research, an outdoor temperature of 50 °C and solar irradiance of 1,250 W/m^2 are used as the worst outdoor condition.

Thermally speaking, the biggest concern for the outdoor digital displays resides in the display face including the vandal glass, LCD, and light emitting diodes (LED). Under a direct sunlight, the solar irradiance gets absorbed by the vandal glass and LCD which has a significant heating effect independent of the outside temperature. From the inside, not only electronic components such as fans or circuit boards introduce a moderate heat,

but also the LED itself consumes significant power which is introduced to the adjacent heat sink and partially gets dissipated through an air gap located between the optical films and LED. The resulting heat in the display face may have a detrimental effect on the LCD as an exposure to high temperature can cause a solar clearing, a phase change in liquid crystals which leads to an appearance of black blotches or complete blackening of the display as seen in Figure 2 [4].

To prevent such phenomenon to take effect on the LCD, the outdoor digital display examined in this research utilizes an air-to-air heat exchanger that uses external ambient air (open-loop), while the internals of the display are completely sealed and the internal air (closed-loop) circulates within to generate additional convective cooling effect but does not mix with the open-loop air [5]. In Chapter 2, a short review on viable types of cooling methodology for the outdoor digital displays is made along with a detailed explanation on the mechanism of the heat exchanger using the closed-loop and open-loop. In addition, two types of display configurations involving the LCD and backlight are described: edge-lit and direct-lit. The benefits of each display configuration and how this affects the thermal performance of the outdoor digital displays are discussed.

In Chapter 3, the simulation setup, mainly done by using ICEPAK from ANSYS, is described along with procedures of outdoor testing used for the validation and extrapolation purposes. As the original intention of the research is to predict the thermal performance of the outdoor digital displays under the worst outdoor condition, the simulation setup for such case is first described. Throughout the research, it is shown that the only radiation model in ICEPAK that is capable of handling semi-transparent material

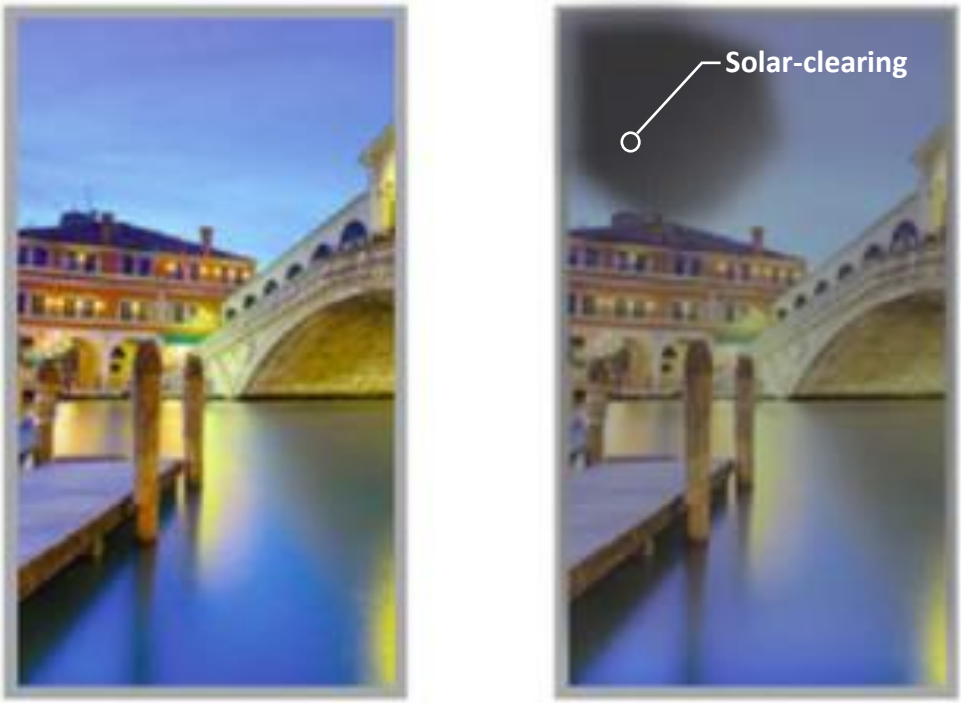

Figure 2 – A picture of a normal LCD screen and an LCD screen under solar-clearing effect [4]

is discrete ordinates model and with limited resources on the radiative properties of the materials, and inclusion of multiple surfaces in a domain, such model often yields misleading results. Thus, a unique methodology to replace the solar irradiance (W/m^2) in terms of power (W) in the sun-sided display parts is described. The outdoor testing is performed to obtain number of ambient temperature and irradiance data points which are used later in the simulation as boundary conditions. Along with the outdoor testing, for the solar irradiance replacement, true solar testing is conducted which uses pyranometers to determine the ratio of initial solar irradiance that gets absorbed by the display components.

A total of three distinct display units are examined in this research: 55” outdoor digital displays with 3,500 nits and 6,000 nits brightness and 98” outdoor digital display with 3,500 nits brightness where the leading number denotes a diagonal length of the display and ‘nit’ or ‘candela per square meter’ is a unit of measurement of luminance. In Chapter 4, CFD/HT simulation on 55” outdoor digital displays are performed, and the results are validated and compared with the experimental results at the obtained outdoor conditions. As the main focus of the thermal modeling is on the temperature prediction of the LCD, the CFD/HT results are compared with experimental results specifically throughout the LCD cell. This research examines any result dependency on the grid patterns, meshing techniques and simulation packages.

Regardless of the ambient temperature and solar irradiance settings, it is seen that the simulation from Chapter 4 shows higher temperatures than the experimental results. Such outcome allows the simulation result to be used as a conservative measure for thermal design of the product but even when mesh count is high enough to guarantee a grid independence of the simulation, the error between the two remains around 2 °C to 5 °C throughout the LCD surface [6]. This error may not only be a consequence of numerical error but also an outcome of simplifications and assumptions involved with the simulation.

One of the key aspects that could be reconsidered to minimize such error resides in the heat distribution in the vandal glass which is heavily affected by the solar irradiance. The initial simulation done on the outdoor digital displays assumes that the solar irradiance on the semi-transparent vandal glass is distributed evenly in each layer of the vandal glass. In Chapter 5, in lieu of even heat distribution along the vandal glass, the

resulting heat is reallocated in a way to provide more accurate and realistic simulation results.

Given that the CFD/HT simulation result shows a conservative approximation of thermal performance of the display, the same simulation setup and method can be used to see how the change in material or geometry can affect the thermal performance of the digital display. Out of all display components, it turns out that the LCD temperature reaches the closest to its limit under the worst outdoor condition. In Chapter 6, out of many parameters that can be touched on, the closed-loop air gap located in between the vandal glass and LCD is adjusted for the following reasons:

1) Optimization of the thermal performance in the display face to minimize the LCD temperature
2) Examination of the LCD temperature rise in case the gap distance changes due to outer source

As it is observed that the LCD bends outward due to the body force and system pressure inside the display, a parametric study is conducted to observe how much of a deflection can cause a significant temperature-rise in the LCD.

Lastly, in Chapters 7 and 8, the thermal modeling of a 98” outdoor digital display is done where a deflection in the LCD is accounted for geometrically. A conclusion and future directions for this research are made.

CHAPTER 2. BACKGROUND AND LITERATURE REVIEW

In this chapter, relevant background and overview of outdoor digital displays are described. The two most dominant LED backlight configurations are presented along with positives and negatives of each configuration. A general set of cooling methods in use for the outdoor digital displays is described.

2.1 Backlight unit configurations

LCD technology has been widely used in the commercial display market because of its remarkably low cost and its ability to produce slim and large-size displays. As LCDs do not produce light by themselves, backlighting is required to output a visible image. In early years, cold cathode fluorescent lamp (CCFL) backlighting was dominantly used in LCD panels but due to low contrast ratio and excess heat arising from conventionally illuminating the entire area of the display at all times of operation, a local dimming technology using LED has been commonly used in the backlight unit (BLU). Through local dimming, the BLU illuminates only when and where the light is required, thus dramatically enhancing both the LCD's contrast ratio and energy efficiency [7]. Since the introduction of local dimming in the BLU, the LED has grown consistently popular [8, 9].

The two most widely used backlighting configurations using LEDs are edge-lit and direct-lit. For the indoor and outdoor digital displays, one configuration is preferred over the other due to a difference in brightness output; about 500 nits would be sufficient enough to ensure indoor readability but a minimum of 1,000 nits is required for outdoor

sunlight readability [10]. Due to the need of higher brightness and thermal problems introduced in consequence to such need, direct-lit BLU is preferred over edge-lit BLU for outdoor uses. Details on each configuration are provided in the below sub-sections.

2.1.1 Edge-lit backlight unit

In edge-lit BLU, the LEDs are placed either on one, two, three or around entire perimeter of the LCD screen as displayed in Figure 3. The light projected from the LEDs is eventually spread out across the display through a light guide panel and optical diffuser plates. Edge-lit BLU has been commonly used in indoor digital displays due to its nature of providing a compact packaging with low thickness overall [11]. However, due to the light emitting circumferentially, local dimming is not as effective as in direct-lit BLU and if the LCD screen is large enough, the center of the screen would appear darker than its edge in some cases [12]. Not only there are limits in providing a uniform brightness, edge-lit BLU is a poor choice when thermal challenges residing in the display is at high risk. As the LEDs are localized in the perimeter, the LCD faces inevitable overheating in its sides as seen in Figure 4 [13].

2.1.2 Direct-lit backlight unit

Compared to the circumferential placement of LEDs in edge-lit, direct-lit is characterized by a placement of LEDs behind the LCD, distributed over the entire screen as shown in Figure 3. Since the light from the LED is projected normal to the screen, a diffuser plate is placed without a need of a light guide panel. In this configuration, direct-lit BLU provides evenly distributed high brightness over the screen with an effective local dimming that edge-lit BLU cannot achieve [14]. Unfortunately, direct-lit BLU ends

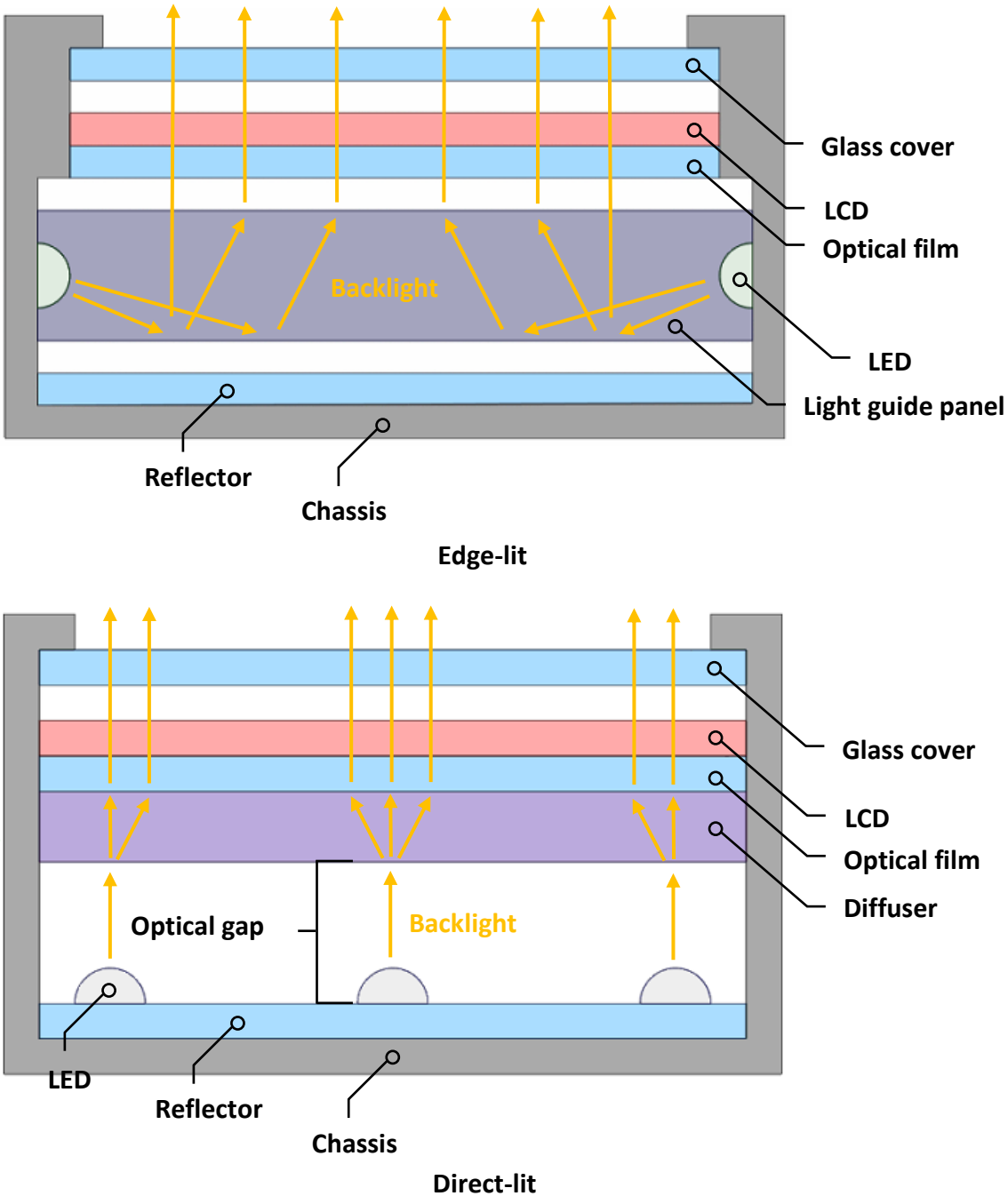

Figure 3 – Direct-lit and edge-lit backlight LCD panels (not to scale)

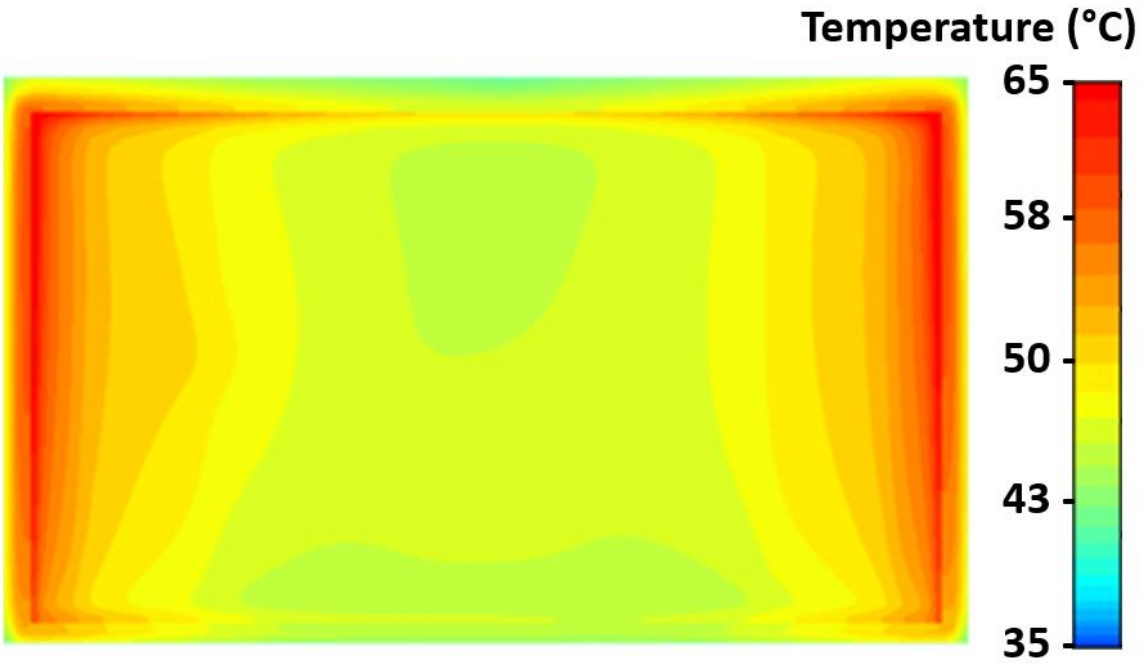

Figure 4 – Calculated temperature distribution in a left and right edge-lit TV [11]

up being comparatively thicker than edge-lit BLU as the LED array must be kept at a specific distance from the diffuser plate in the backlight module, which is also known as an optical gap or optical distance [15]. Due to the natural convection effects in this gap, the heating effect is inherently non-uniform, but still the heating effect is not as localized as in edge-lit BLU as shown in Figure 5 [13]. Even with less localized heat distribution in direct-lit BLU, hotspots due to the heat dissipation in LEDs impose thermal challenges, especially for the screen display in the open environment. Many studies investigate ways to minimize the thermal failure in LCD and LED configurations ranging from placement methods including PCB and cooling boss to optimization of reflector patterns [16, 17].

2.2 Thermal management of outdoor digital displays

It is known that only a fraction of the electrical input power to the LED is converted into light, and the remainder converts to heat, requiring removal through

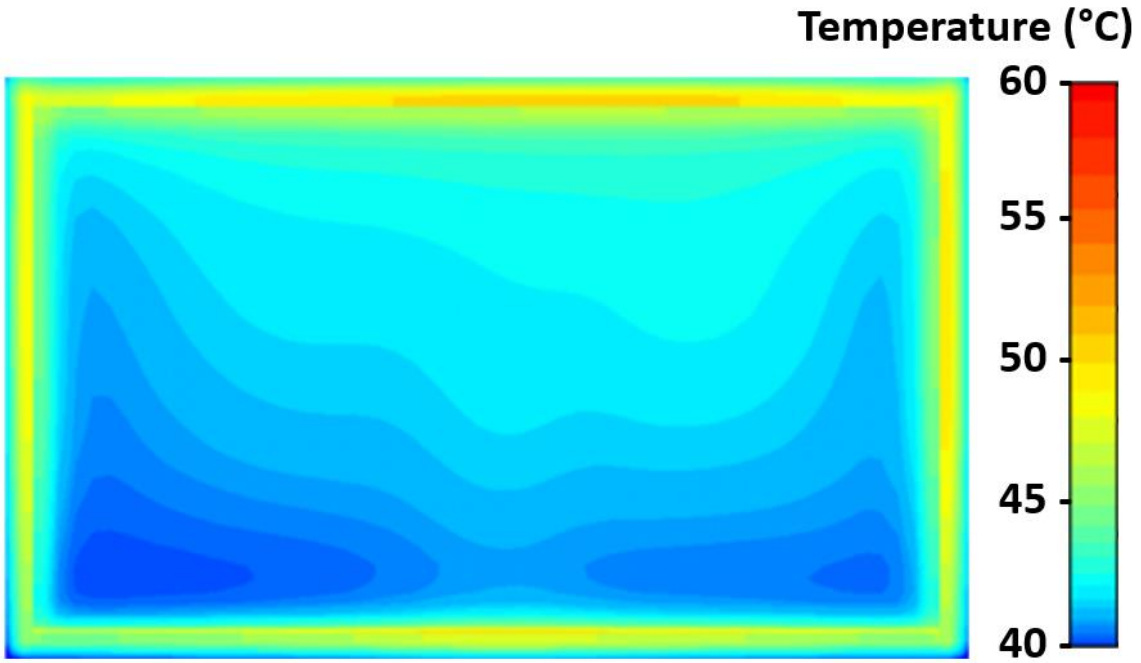

Figure 5 – Calculated Temperature Distribution in a direct-lit TV [11]

thermal management [18]. Thermal management of BLU can range from the use of natural convection to the use of liquid cooling loops that allow for enhanced heat removal compared to the traditional gas cooling using air. In the outdoor digital displays, the use of natural convection and forced convection using air as a medium have been common, as liquid cooling may not be suitable for this particular case [19]. In this section, a description of a possible cooling concept for the outdoor digital displays is provided that may involve fans, blowers, air-to-air heat exchangers, air-conditioners, and other cooling techniques. One specific type of cooling method currently used in the outdoor digital displays discussed in this research is introduced in detail.

2.2.1 Active and semi-active cooling

Thermal management in the outdoor digital displays can be categorized based on the involvement of the ambient air in the cooling method. An active thermal management

approach is defined by a sealed digital display which utilizes internal cooling mechanism to keep the system temperature and the display temperature below a prescribed limit. This approach does not allow any of the sensitive display components to make a contact with the outside air which is the main cause of corrosion or impurity in the screen and is advantageous in a way that no air filter or maintenance to replace the filter is required. However, high dependency on the internal cooling devices to meet the thermal requirements results in higher electricity consumption and perfect sealing of the display unit that causes undesirable robustness of the overall unit dimension [20].

A semi-active thermal management, which is an improved version of a passive cooling method that does not require expenditure of electrical power to provide thermal management, uses forced convection through the ambient air that is certain to be at lower temperature than the display unit for the BLU cooling [11]. Forced convection by fans is utilized in this case where the fans would be placed in the perimeter of the optical gap to minimize the heat dissipation in the LEDs projecting onto the diffuser plate or the optical films. This approach requires less power consumption, yet the use of air filter and regular maintenance becomes necessary for sustainability. This approach also limits the LCD configuration as the outside air entering the electronics cabinet may cause a problem if the LCD panel is not optically bonded to cover glass. If there is any space between the LCD and the front glass of the display, outside air may condense between the display and the glass, obscuring the display [21].

2.2.2 Open-loop and closed-loop cooling

To overcome the thermal challenges, the outdoor digital displays discussed in this research utilize semi-active thermal management system to keep the system temperature within an acceptable range. In the two parts of the heat exchanger, one utilizes the hot air trapped internally for convective cooling and the other utilizes the cool ambient air to further enhance and assist the convective cooling effect.

The closed-loop of the heat exchanger uses internal fans placed in the chassis of the unit which circulates the air around the unit. The internal air which is always trapped inside the unit due to sealing, follows the trajectory shown in Figure 6 which enters the optical gap and air gap between the LCD and the vandal glass to assist in effective heat dissipation. The open-loop of the heat exchanger uses fans placed either on top or bottom of the unit that introduces the outside air which is going to be at lower temperature than the unit system temperature. The air enters a vent located between the LED junction and the chassis as seen in Figure 7 so that the heat from LED can be removed while the air does not flow into the sensitive displays [5]. In this way, while the content of the display is kept as transparent as possible with little to no impurity in BLU and no maintenance is required for air filter exchange, the power consumption within the unit can be kept relatively small. Through CFD/HT simulation, the thermal performance of the outdoor digital displays with open-loop and closed-loop cooling mechanism is evaluated in later chapters.

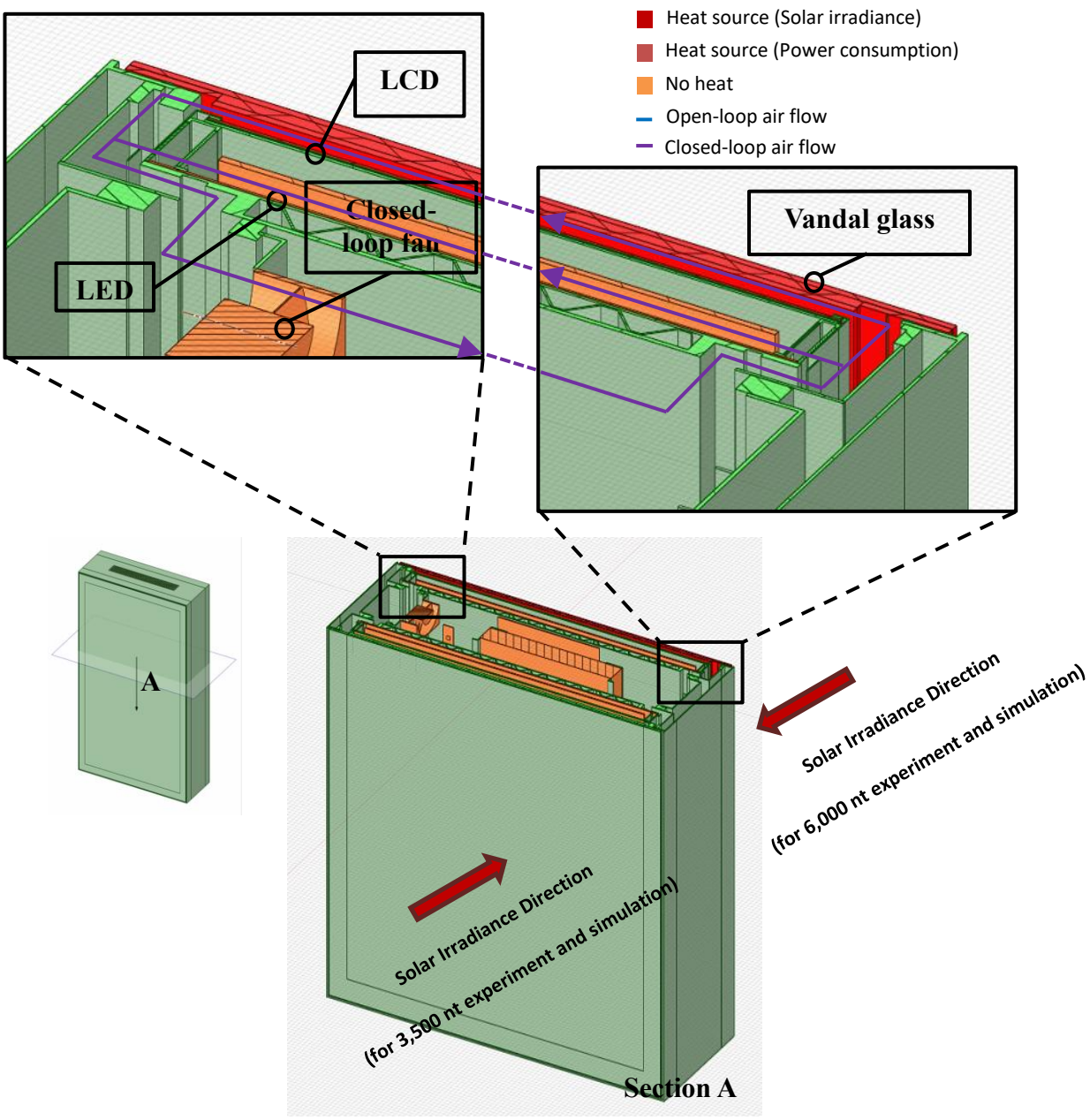

Figure 6 – The closed-loop of the heat exchanger for a 55” outdoor digital display

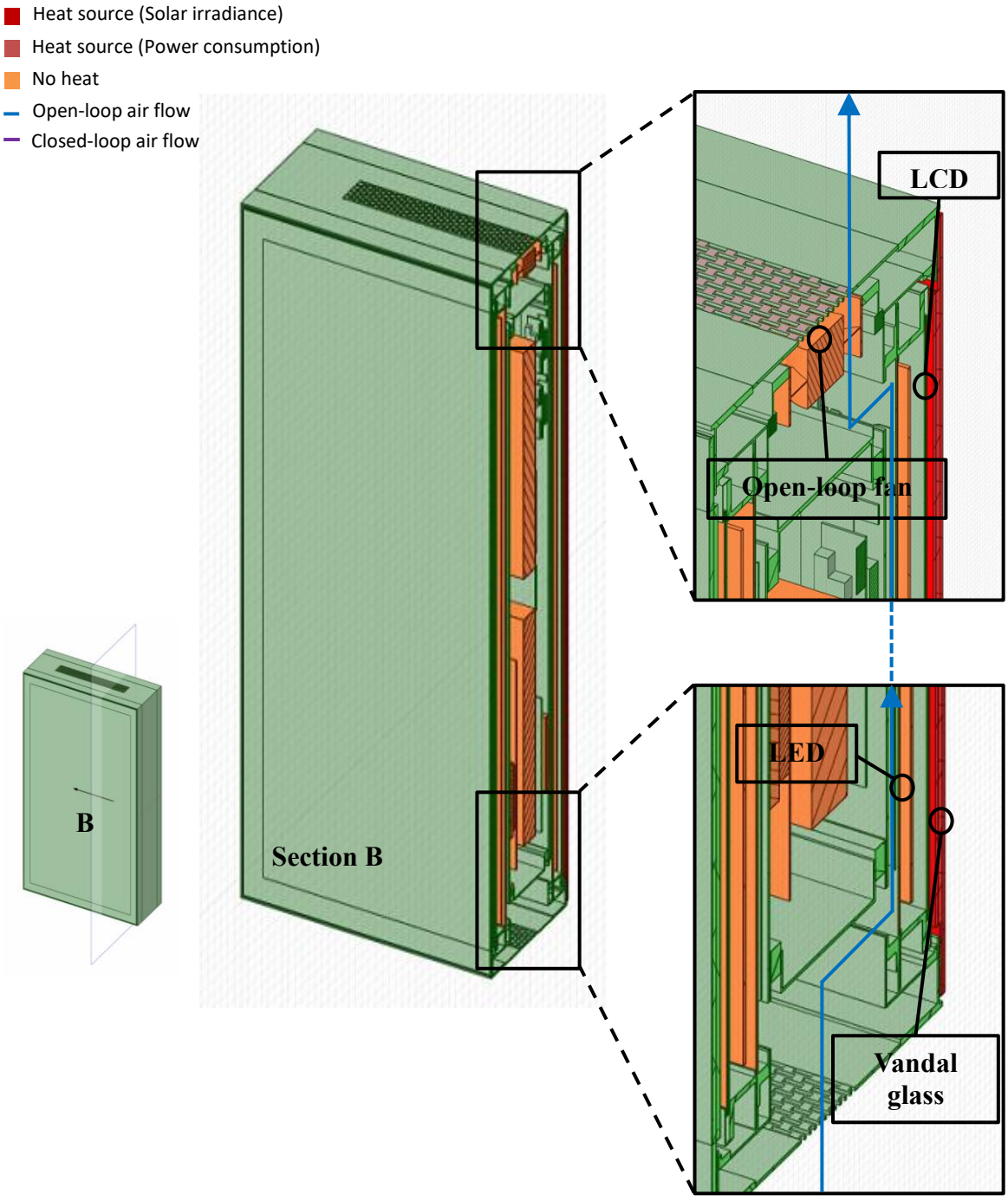

Figure 7 – The open-loop of the heat exchanger for a 55” outdoor digital display

CHAPTER 3. EXPERIMENT AND SIMULATION SETUP

In this chapter, the outdoor testing of 55" outdoor digital displays is presented along with the setup of the simulation used throughout the research.

3.1 Experiment for simulation data collection

In this section, the procedure and method of the outdoor testing conducted over two days are described. The first was performed on February 9th, 2018 for 3,500 nits display and the second was performed on December 11th, 2018 for 6,000 nits display at Manufacturing Resources International (MRI) testing site located in Alpharetta, GA. Beside the outdoor testing that is used to monitor the LCD temperature at selected locations, a separate testing so called 'true solar testing' is performed to approximate the proportion of solar irradiance that gets absorbed by the vandal glass. The results from two testing are later utilized in the simulation.

3.1.1 Outdoor testing of 55" outdoor digital displays

Due to heavy heat loads from solar irradiance and internal heat generation, should the outdoor digital display fail thermally, it is expected to happen in the LCD cell. To capture the variation in the LCD temperature due to the incident solar irradiance, a 55" outdoor digital display is positioned so that one of the display faces would be exposed to the sun normal during sunrise. The display unit during the day of testing is shown in Figure 8. To keep the spectral content of solar irradiance realistic, the testing is performed on a cloudless day with no shade interfering with the unit. The sun-sided LCD temperatures at six different locations (L1 to L6) are measured by placing thermocouples,

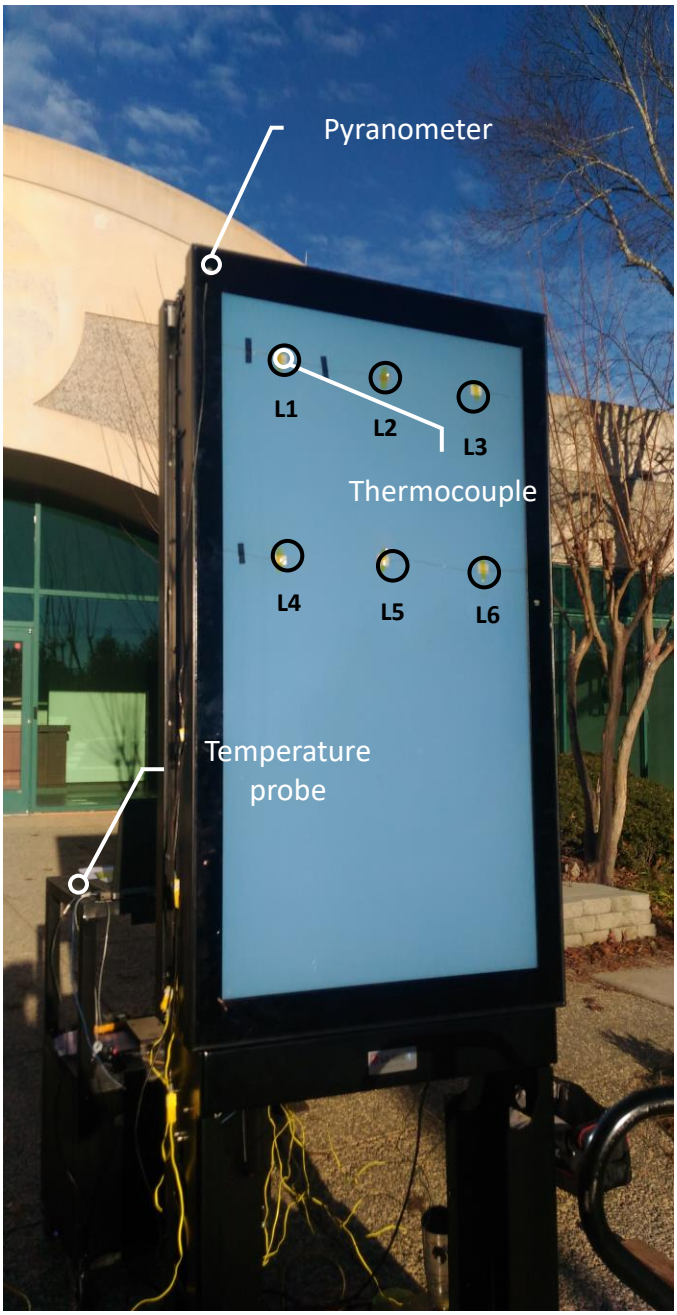

Figure 8 – Outdoor testing of a 6,000 nits 55" outdoor digital display

SA3, on top and middle portion of LCD screen in an open space of air gaps of 8mm and 33mm in upright position. The solar irradiance projecting onto the LCD is captured throughout the testing by placing a pyranometer, Apogee SP-420, on the top left corner of the vandal glass which measures global shortwave radiation normal to the screen surface

in the wavelength range of 280 nm to 4,000 nm. It should be noted that while the pyranometer only measures the normally projected solar irradiance, the display face takes the solar irradiance from any angle. Some of the initial solar irradiance projected on the ground may get reflected and be introduced to the display face. It is known that the amount of ground-reflected solar irradiance can vary depending on albedo, a proportion of incident irradiance that gets reflected, for a typical asphalt, around 4% of the irradiance gets reflected [22]. Lastly, an ambient temperature probe is placed in an open space to monitor the outdoor temperature. The specifications for the apparatus used in the outdoor testing is listed in Appendix A.

3.1.2 True solar testing of the vandal glass

As mentioned earlier in Chapter 1, the simulation requires special consideration when multiple semi-transparent materials are included in a domain and solar loading is set as a heat flux. To best account for the impact of the solar irradiance, the solar irradiance is replaced with a heat load in terms of power in the sun-sided display components by approximating how much of the input irradiance gets absorbed by each component.

To obtain the absorption factor of the vandal glass, which is used later in the simulation, a pyranometer, is adhered to a black tabletop, surrounded by a black shroud. Second pyranometer is placed on the bottom of the shroud. First, the vandal glass is cut in an adequate size for the testing: 15 cm by 15 cm in length and width. The sample is then placed on the black shroud as shown in Figure 9. The first pyranometer reading is recorded prior to the placement of the vandal glass to measure the initial solar irradiance.

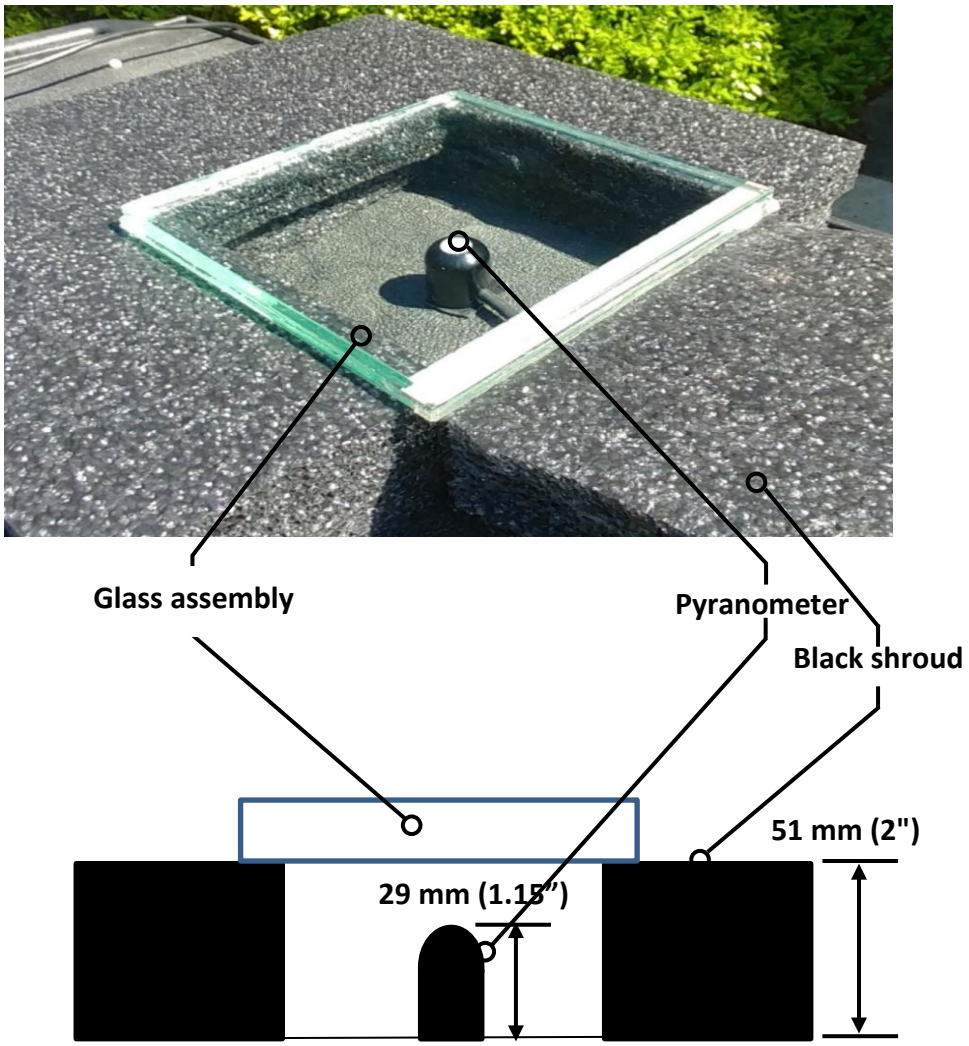

Figure 9 – True solar testing setup

The second reading is followed up by measuring the irradiance after the placement of the vandal glass which gives out the transmitted solar irradiance. Data are recorded multiple times to assure consistency. The true solar testing was conducted in Alpharetta, GA on May 2nd, 2019.

3.2 Initial simulation setup and settings

In order to best reflect the outdoor condition in CFD/HT simulations, the computer-aided design (CAD) model of an outdoor digital display is set at the centre of a

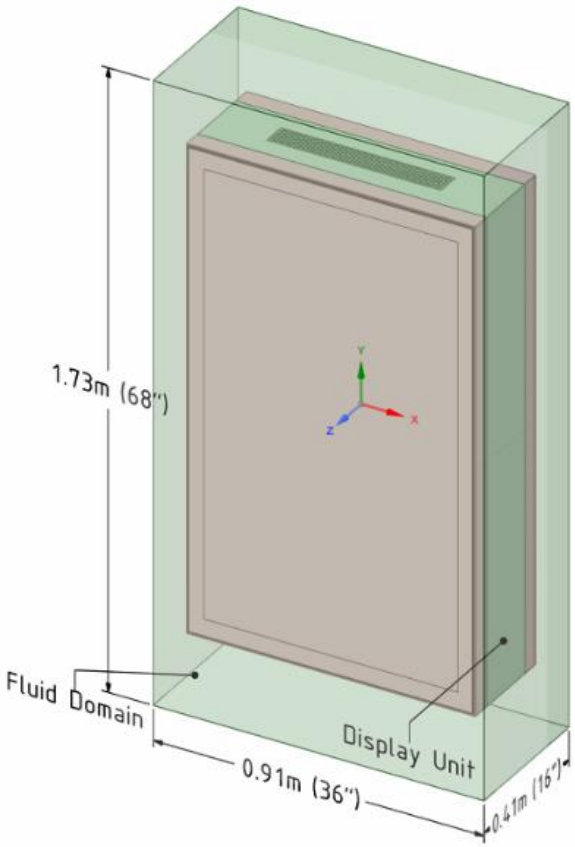

Figure 10 – Domain setup for a 55" outdoor digital display simulation

fluid domain, set large enough to completely enclose the display, and extending 0.5 m in consideration of natural convection on the vandal glass, the ambient environment, and the fluid domain, marked as a green cuboid in Figure 10.

A total of eight materials are used in the simulation, which include air, aluminum, polycarbonate, heatflow sil-pad, glass, printed circuit board, insulator, and silicon. Assuming the outdoor digital display is operating at its maximum output, the heat loads due to power consumption in electronic components and fans are assigned as defined in the guideline. An additional 150 W of power consumption is assumed in two sets of user equipment boxes placed at the center of the display, in consideration of worst-case scenario. In two display faces joined by the chassis, major heat loads are set, which

largely come from the LED. For LED tiles in the backlight, the applied power is determined based on several factors (i.e. transmission through vandal glass, transmission through optical stack, power consumption necessary for the desired brightness of the display). To achieve a desired brightness of 3,500 nits for sunlight readability in 55" digital display configuration, 248.7 W of power is supplied to the LED tiles which increases to 506.5 W to reach an even higher brightness of 6,000 nits. The actual LED tiles are made of an aluminum substrate with the LED array located on one side and total of 4 tiles are present per display. For the simulation, the tiles are assumed to be a single component. The input power to the LED tiles is determined empirically where ~70% of the power is dissipated as heat in the LED tiles themselves. The remaining ~30% of the input power to the LED tiles is assumed to be absorbed by the air in the backlight cavity (an air gap between the LCD and LED) [6].

On the sun-sided display face, normal projection of the solar irradiance is assumed. In lieu of imposing solar heat flux on one of the boundary surfaces, the thermal contribution of solar irradiance is expressed using the absorption factor, η, obtained from true solar testing. The heat load on the sun-sided display components follow the below equation:

$$Q = \eta \cdot G \cdot A \tag{1}$$

where G is the solar irradiance, and A is the surface area normal to the sun. From true solar testing, it is shown that 26% of the initial irradiance gets absorbed by the vandal glass. Approximate heat load on the vandal glass is obtained by using Eq. (1), but it is important to note that the vandal glass is a lamination of multiple glass layers and

Table 1 – Heat loads due to the solar irradiance on a 55” display

PART NAME	ABSORPTION FACTOR	AREA (M^2)	IRRADIANCE (W/M^2)	HEAT LOAD (W)
GLASS MASK	0.79	0.2185	1,250	215.7
VANDAL GLASS	0.26	0.8250	1,250	268.1
LCD	1.00	0.8250	925	763.0

adhesives. The obtained heat load is assumed to be evenly distributed in these layers for the initial simulation conducted in this research. For 74% of irradiance that is not absorbed by the vandal glass, it is assumed that the LCD, which is next closest to the sun, absorbs the rest to obtain a conservative simulation result. Additional heat loads due to the solar irradiance on the sun-sided display face are listed in Table 1.

For three closed-loop and two open-loop fans used in 55” outdoor digital displays, dynamic fan curves are used at their maximum duty cycle. The swirling effect on fans is taken into account under their maximum performance of 9,700 RPM and 8,500 RPM for closed-loop and open-loop fan, respectively. For the boundary condition settings, a fixed temperature of the surrounding air is assumed on four side surfaces. A set of simulations is performed using adiabatic wall boundary condition and pressure far-field boundary condition, but all had an insignificant effect on the results; for faster solution convergence, a fixed temperature is selected. In the case of 55” outdoor digital displays, two open-loop fans placed on the top surface of the digital display pull the air from the bottom, so pressure inlet is assumed on the bottom side of the fluid domain and pressure

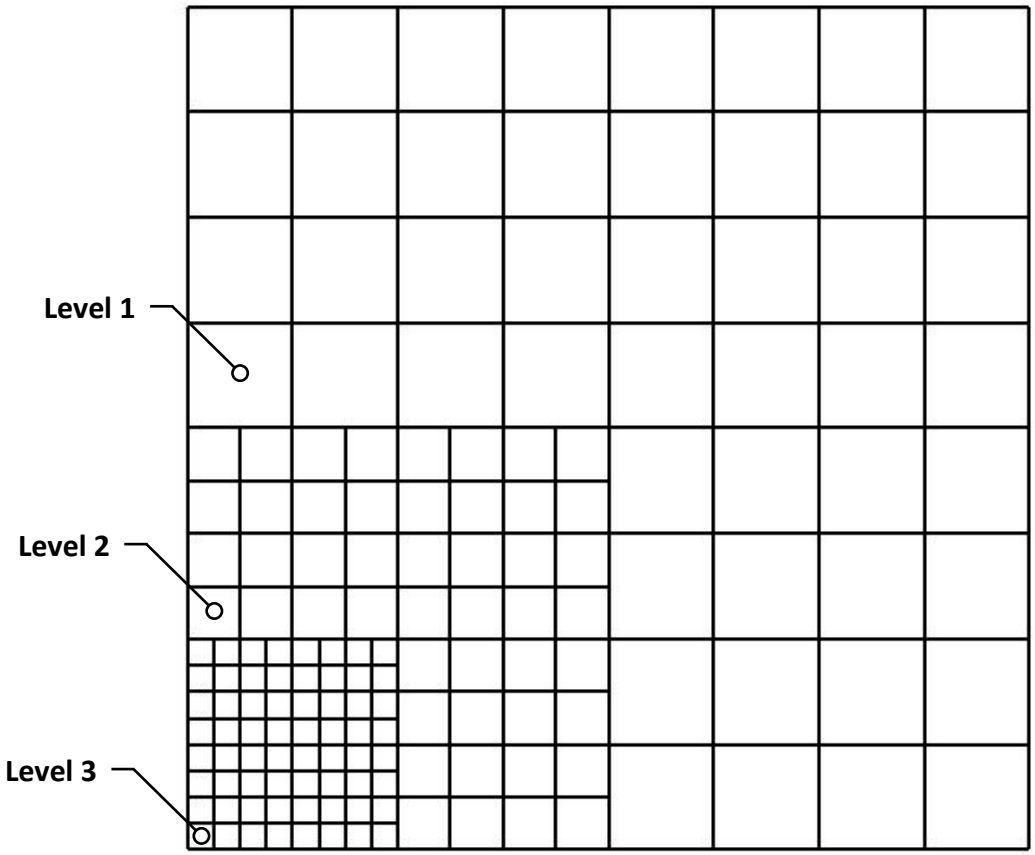

Figure 11 – Cartesian mesh refinement via multi-level

outlet is used accordingly on the remaining top side of the fluid domain [23]. For 98" outdoor digital displays, open-loop fans are placed on the bottom surface and pull the air from the top, so a pressure inlet is assumed on the top boundary surface. The inlet air temperature is set equivalent to the outdoor temperature for all cases.

As one of the main goals of this research is to compare the results between different simulation packages, an effort to match the mesh outline is made. Both ICEPAK and FloEFD share a similar meshing scheme in which, in lieu of tetrahedral, hexa-dominant meshing is used. As the simulation domain extends up to 2 m in height, multi-level meshing is effectively used, which enables local refinement from a starting cartesian mesh generated using the maximum sizes specified (see Figure 11) [24]. Unlike

FloEFD, where solid parts are prioritized over fluid parts when the mesh is overlapped in between, ICEPAK tends to omit the solid parts when an insufficient refinement setting is assigned. To minimize such effect and ensure that the closed-loop air does not escape to the ambient, non-conforming mesh is used complimentary to the multi-level meshing. For all simulations, a minimum of three elements are assigned for every fluid gap. In each package, the turbulence model is set to RNG k-ε, and the radiation model is set to ray-tracing (see Appendix B). For solution convergence, the built-in residual criterion is used: 1E-3 for continuity, kinetic energy and dissipation rate, and 1E-7 for energy. As the simulation could still diverge after meeting the residual criterion, additional iterations are performed until the residuals would reach a steady value.

Using the above setup, the first simulation is performed for the worst outdoor setting. After obtaining a converging solution from the first simulation, additional simulations are conducted with different ambient temperature and irradiance settings. For these simulations, the ambient air and surrounding temperature are set equivalent to the outdoor temperature as measured during the experiment, ranging from 1 to 20 °C. The simulation setup is kept the same besides the input power necessary to meet the backlight brightness and the emerging heat from solar irradiance where the sun is assumed to be projected from the left side of the display in Figure 6 for 3,500 nits display and from the right side for 6,000 nits display.

A set of simulation is performed to examine the effects of grid size and the difference in the results of conforming and non-conforming mesh. Using non-conforming mesh to effectively reduce the total element and node count, while allocating high grid density in the regions of high pressure and temperature gradient, the mesh is generated

ranging from 3 million to 13 million elements. As the use of non-conforming mesh results in incompatibility due to approximations in shape functions, the data variance between the non-conforming and conforming mesh technique is compared to observe the consequence of non-conforming mesh in macro-scale CFD/HT simulation.

CHAPTER 4. SIMULATION RESULTS ON 55” OUTDOOR DIGITAL DISPLAYS

In this chapter, CFD/HT simulation based on the setup discussed in Chapter 3 is performed on 55” outdoor digital displays and the results are discussed. The initial simulation focuses on the thermal performance of the display under worst outdoor condition of 50 °C ambient temperature and 1,250 W/m^2 solar irradiance. Experimentally obtained outdoor settings at various ambient temperature and irradiance are then used in the simulation where the results are compared with the outdoor testing results to show how they correlate. The simulation dependencies on grid size, meshing technique and software are discussed in addition to examine reliability of the simulation results.

4.1 3,500 nits brightness results

This section focuses on CFD/HT results of a 55” outdoor digital display with 3,500 nits brightness output. As in the outdoor testing, the solar irradiance is projected on the left side of the display in Figure 6, and the heat loads due to the solar irradiance using Eq. (1) are imposed on the left side of the display.

4.1.1 Hazardous outdoor setting

Prior to the experiment and simulation that are used for validation, a simulation on a 55” outdoor digital display under the worst outdoor setting is performed. In Figures 12 and 13, the velocity vectors inside the closed-loop and open-loop of the heat exchanger are shown to see how the convective cooling takes place. As described in Chapter 2, closed-loop air that has been pushed to the end of the chassis enters the

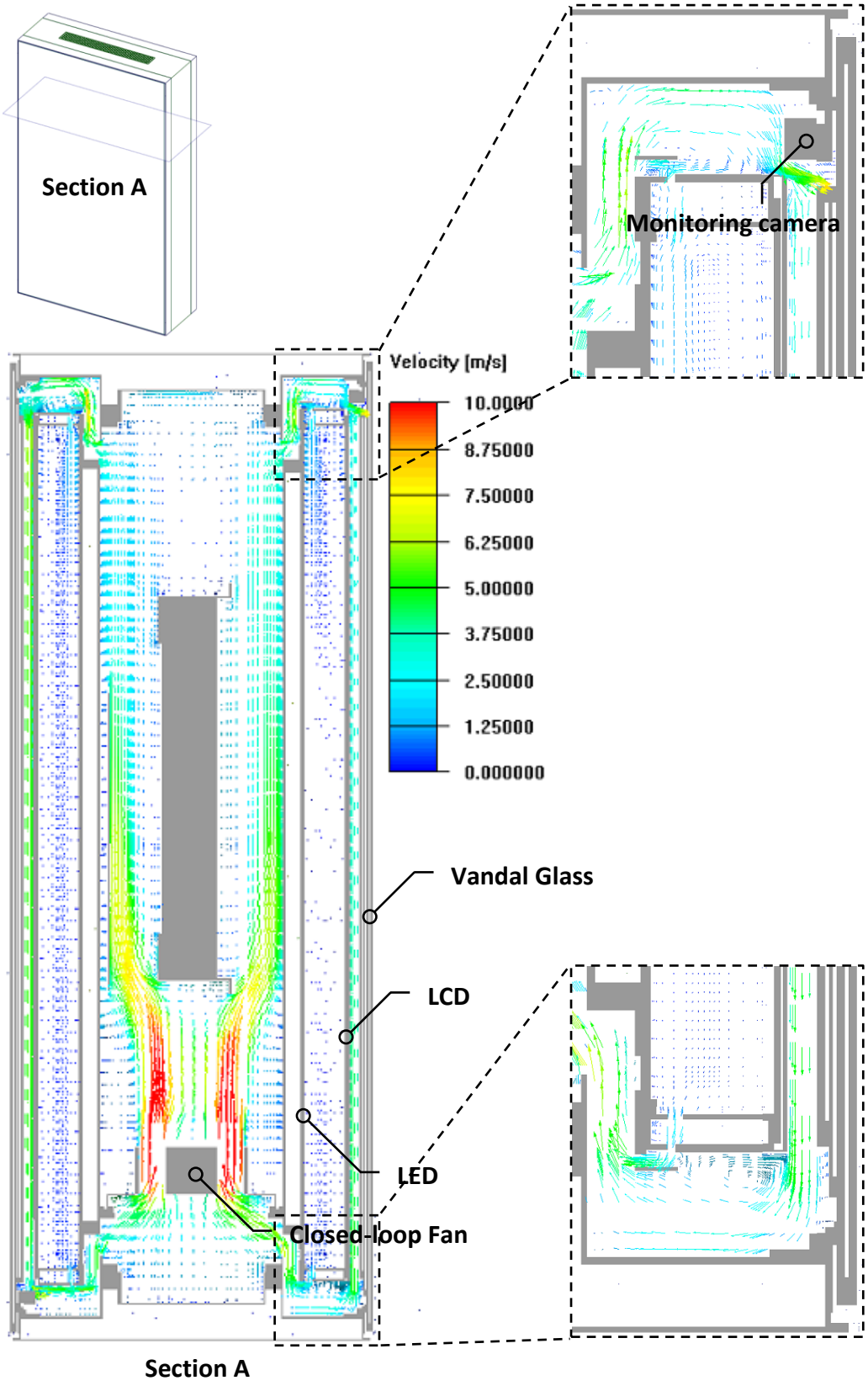

Figure 12 – Air velocity vector of the closed-loop of the heat exchanger

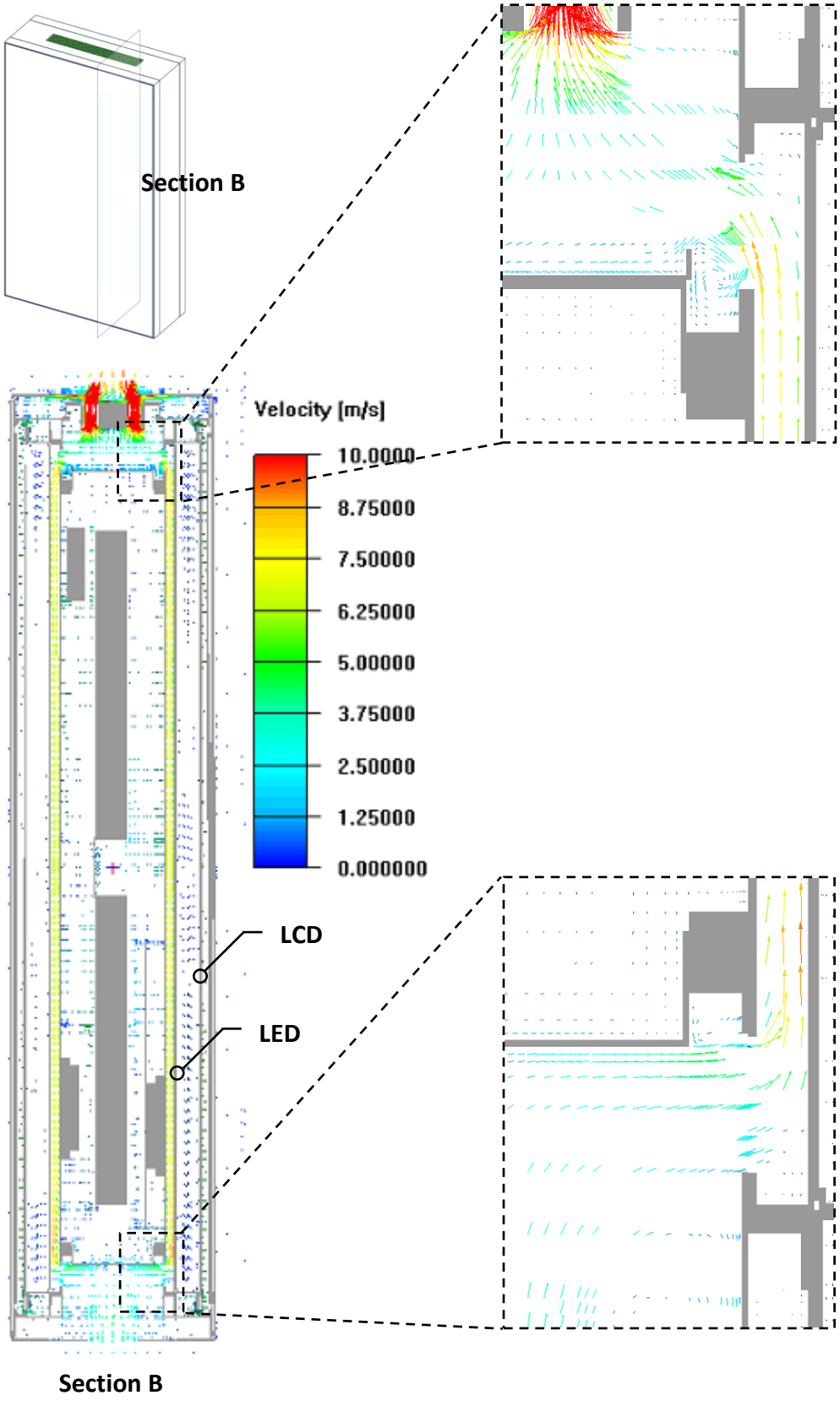

Figure 13 – Air velocity vector of the open-loop of the heat exchanger

opening connected to the display face and makes its way to the optical gap and closed-loop gap. Averaged over cross-sectional area of each opening, the air velocity in the entrance of the optical gap is about 2.7 m/s and the closed-loop gap is 7.9 m/s. In the open-loop of the heat exchanger, the air follows the trajectory guided by the passage located between the PCB tile, directly cooling the LEDs placed on top of the PCB.

On the sun-sided display face, the LCD and LED reach a maximum temperature of 103.1°C and 77.1 °C, respectively where the hotspot is located near the top left end as shown in Figure 14. For the sun-sided parts of 3,500 nits brightness display, the closed-loop fan blows the air through the chassis and the streamline follows a trajectory from the right side of the tile to the left side and the convective cooling effect diminishes as the air progresses. The convective cooling effect appears weaker in the hotspot due to the presence of a monitoring camera partially blocking the pathway of the closed-loop passage as shown in Figure 12. The presence of low temperature in the lower region of LCD is due to a similar effect where the open-loop fan blows the air from the bottom to top and most of the cooling effect takes place in the bottom region in addition to the natural convection which traps hot air in the upper section of the display. Due to the small thickness of the tile, the temperature variance in the direction of the thickness could not be observed.

4.1.2 Comparison with outdoor testing

The solar irradiance and ambient temperature data at the day of the testing are collected during the sunrise. Any fluctuating points due to clouds are ignored for the analysis and the remaining data points are used to show the relationship between the

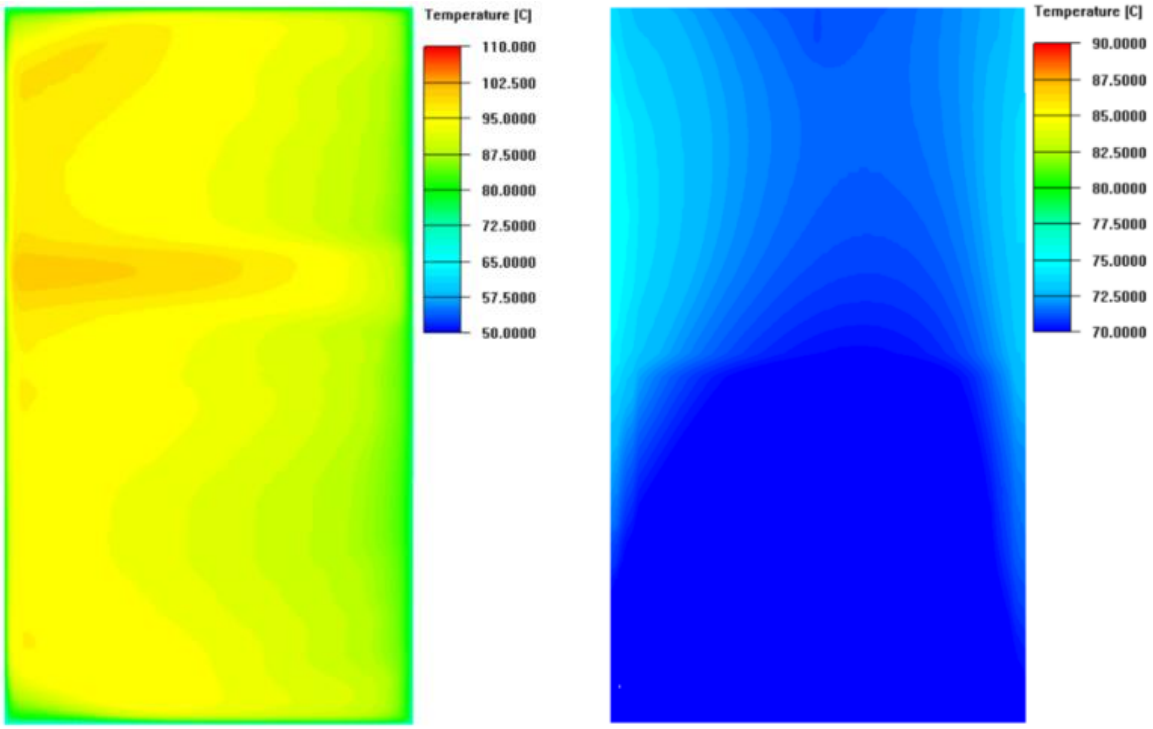

Figure 14 – Temperature contour of sun-sided 3,500 nits 55" display components

temperature of screen components in selected locations and the incident irradiance. Due to variation in ambient temperature, instead of comparing the absolute temperature values, the temperature difference between the display components and the ambient air is used for the comparison. The test results at selected thermocouple locations are marked as dots in Figure 15 where an approximate linear relationship between the relative component temperature and irradiance could be observed.

Tracking the positions of the thermocouples in the sun-sided LCD and other components in the simulation, the temperature data is retrieved and marked as a line in Figure 15. For the LCD, where the solar irradiance was assumed to be completely absorbed, the simulation temperature appeared higher than the experimental temperature at all irradiance settings and thermocouple locations. Specifically, for the two data sets

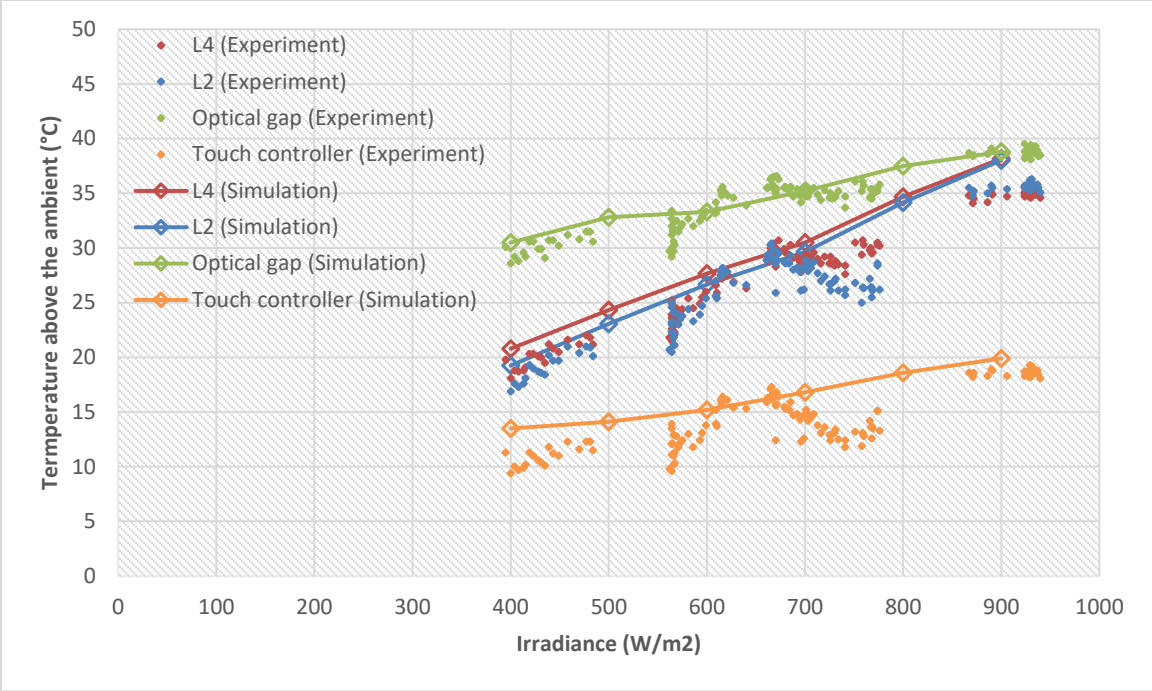

Figure 15 – Relative display component temperature in the outdoor testing and simulation

of the LCD, the temperature at L2 stayed lower than the temperature at L4 under low solar irradiance but grew higher beyond 800 W/m^2 solar irradiance in the experiment. A similar trend could be observed in the simulation where the slope of the linear trend line between the relative LCD temperature and solar irradiance appeared higher for L2. In the remaining display components, close correlation between the experiment and simulation could be observed where the maximum deviation remained at 1.6 °C at the high solar irradiance. In 6,000 nits display, additional thermocouples are added on the LCD to reconfirm how the temperature distribution matches up overall.

4.2 6,000 nits brightness results

This section focuses on CFD/HT results of a 55” outdoor digital display which outputs a higher brightness of 6,000 nits in lieu of 3,500 nits. As in the outdoor testing,

the solar irradiance is projected on the right side of the display in Figure 14, the heat loads using Eq. (1) are imposed on right side components and the location of the hotspot is expected to be reversed.

4.2.1 Hazardous outdoor setting

The LCD and LED temperature contours under the worst outdoor setting of 50 °C ambient temperature and 1,250 W/m^2 solar irradiance are displayed in Figure 16 which indicates that the LCD and LED would reach 104.4 °C and 83.9 °C, respectively. For 6,000 nits display, the sun-side and the air trajectory are reversed, and the hotspot is observed on the right side. Unlike in 3,500 nits display, the hotspot in the middle right corner is not spread in the direction of width as the monitoring camera is placed in the exit of the closed-loop passage for 6,000 nits display. The presence of low temperature in the lower region of LCD is due to a similar effect where the open-loop fan blows the air from the bottom to top and most of the cooling effect takes place in the bottom region in addition to the natural convection which traps hot air in the upper section of the display.

4.2.2 Comparison with outdoor testing

The LCD temperature at the thermocouple locations L1 and L6 is recorded in Figure 17 which showed the lowest and highest temperature throughout the LCD during the outdoor testing. While the difference in temperature-rise at different irradiance settings shows similar trend in the simulation and the experiment, a visible deviation in two results could be observed. The difference in two data sets reaches its maximum under high irradiance where the simulation value turns out to be as high as 6.6 °C at the

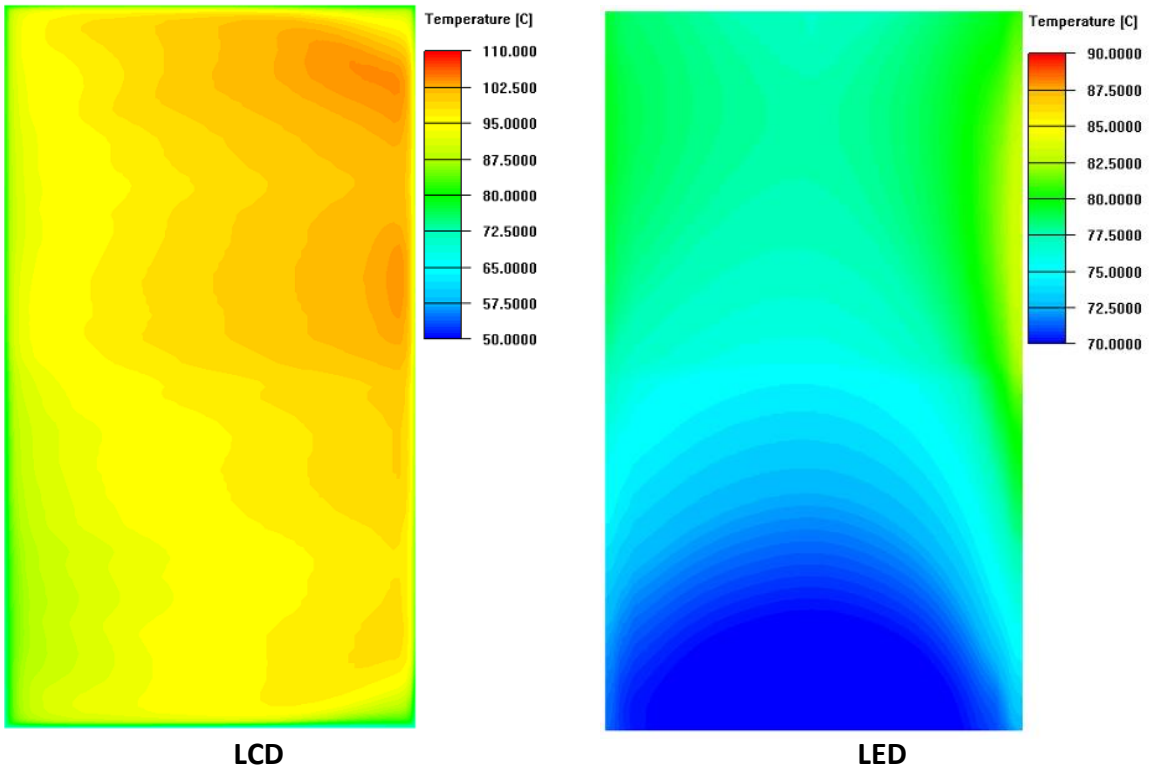

Figure 16 - Temperature contour of sun-sided 6,000 nits 55" display components

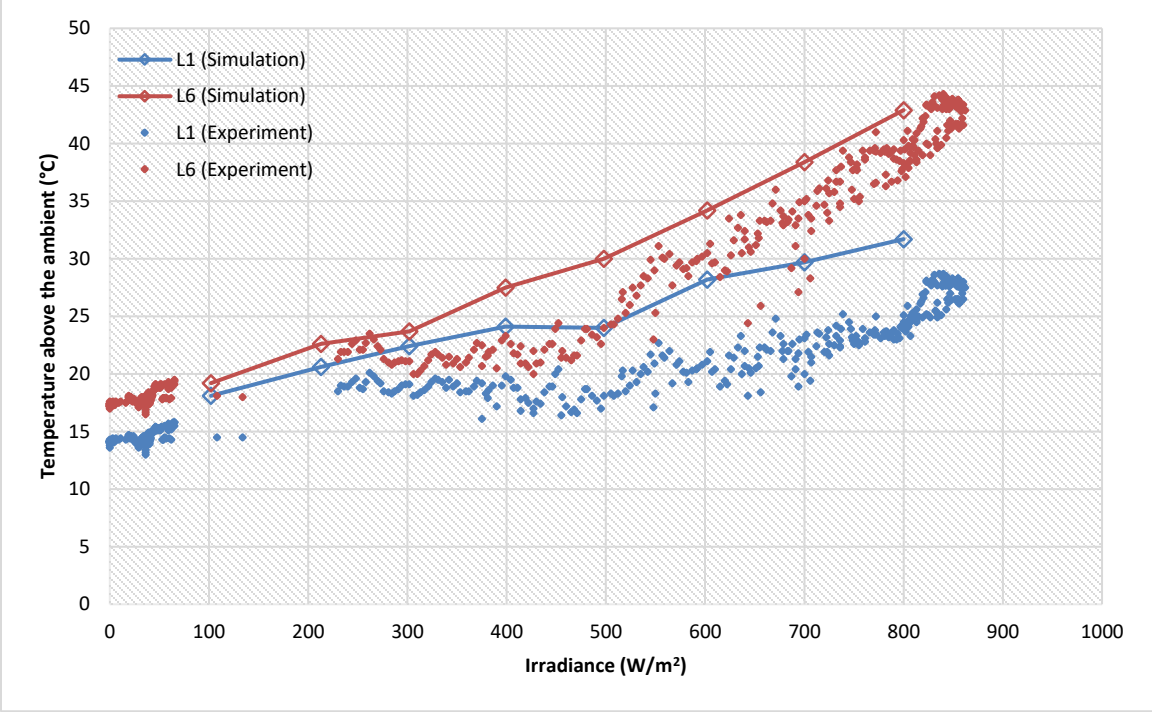

Figure 17 - Relative LCD temperature of 6,000 nits 55" display

location of L1, the coolest region of the LCD. Such mismatch in temperature value is expected to be due to the assumptions involved with the simulation. As the solar irradiance that has not been absorbed by the vandal glass is assumed to be entirely absorbed by the LCD in the simulation, the simulation showed a higher temperature than the experiment.

The mismatch also results from the solar irradiance replacement method where the heat load assigned on the vandal glass, a lamination of multiple glass, was assumed to be evenly distributed on each layer of glass. In reality, higher amount of solar irradiance would be absorbed in the front surface and lesser amount would be absorbed in the later surfaces. Lastly, based on a high temperature mismatch in the cool region of the LCD specifically when the solar irradiance is high, the contribution of the solar irradiance on the display face may not be the same. Since the heat load from the solar irradiance is handled as volumetric heat generation in ICEPAK that evenly distributes the power over the volume of the component, the effect of the solar irradiance near the entrance of the closed-loop passage could be smaller than it is.

To further examine a correlation between the two data sets, the experimental and simulation data at all thermocouple location under 800 W/m^2 irradiance for 6,000 nt display are compared. The highest temperature in both data is observed in L3 and L6 while the temperature at L5 is the third highest. The lowest temperature in the LCD appeared in L1 in the experiment and L4 in the simulation where the simulation temperature at L1 was higher by 0.1 °C; the temperature at L4 was higher by 0.5 °C in the experiment (see Figure 18). Aside from the cool region of the LCD, the temperature distribution in simulation matches with the outdoor test results. As it is for the data

TEMPERATURE DIFFERENCE (°C)	
L1	+6.6
L2	N/A*
L3	+6.5
L4	+6.0
L5	+4.5
L6	+2.6

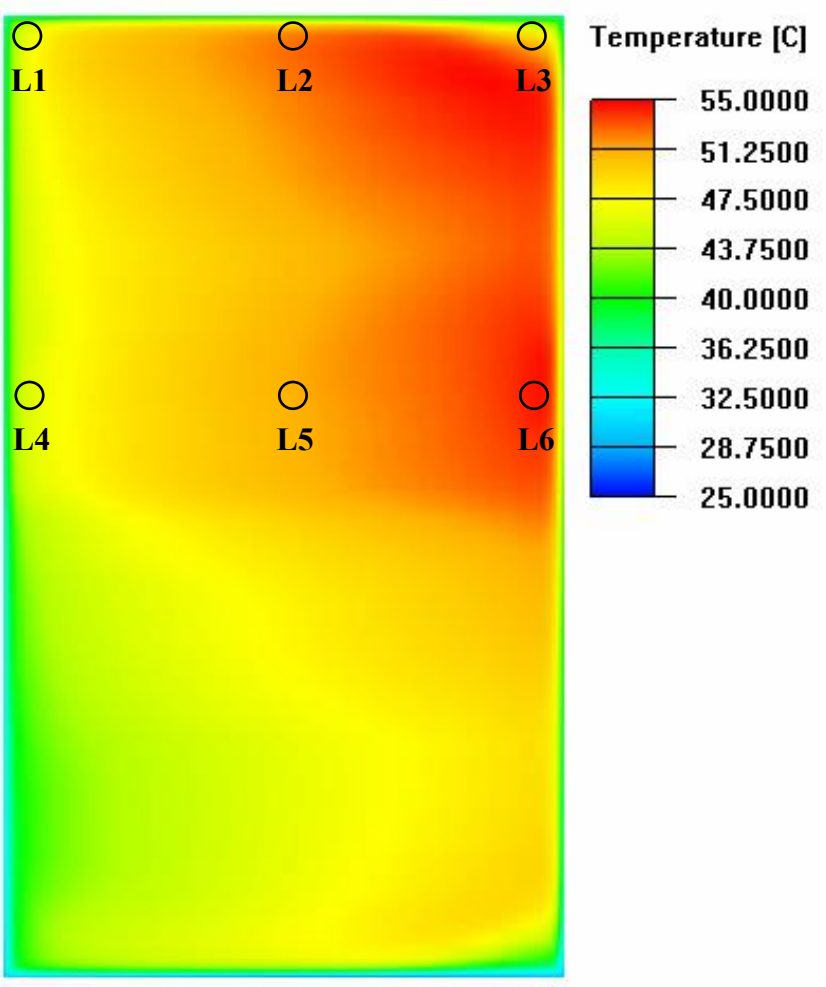

*Temperature data at L2 is unavailable due to the overwrite with the ambient probe data

Figure 18 – LCD temperature difference between the simulation and experiment

comparison at different irradiance settings, the simulation gives out higher temperature at all thermocouple locations, difference reaching as high as 6.6 °C in the cool region and 2.6 °C near the hotspot. Through the use of a finer mesh and realistic approach on the vandal glass heat allocation, better results could be obtained which are discussed in the following section and chapter.

4.3 Grid size study

Another focus of simulation study was to examine the effect of element number in the simulation. As the CAD model of the outdoor digital display is comprised of multiple parts varying as large as 1.4 m to as small as 0.13 mm in length, the solution computation time can take up around 4 hours to over 24 hours depending on the number of elements used to mesh the domain [6]. Thus, for an effective and efficient simulation, it is crucial to look for a specific number of elements that can give reliable results within a reasonable time set.

The simulation results from ICEPAK are shown in Table 2 varying in number of elements from 3.8 to 13.7 million; simulations used for the grid size study are done based on the solar irradiance of 800 W/m^2 and an ambient temperature of 10.5 °C. The absolute maximum temperature of the LCD and LED tile along with the maximum speed and minimum pressure point in the optical gap are recorded. All models are generated with a minimum of 3 elements kept in fluid gaps to ensure the convergence. 3.8 million is the minimum number of elements that is necessary to ensure every solid part is kept in its original form after the meshing process as ICEPAK usually omits or modifies parts according to the specified mesh settings. As the size of simulation and data are vast, there are several criteria to check for the grid size effect. As such, few points are selected near the regions of LCD due to the availability of experimental data in the region and LCD components being the most sensitive to the pressure and temperature effect. As visible from Figure 19, the use of finer elements results in a decrease in maximum temperature and an increase in air speed. Beyond 7.8 million elements, with a minimum of 4 elements kept between a gap, the residual starts to decrease significantly, showing a good indication of convergence [25]. While the maximum values vary depending on the grid

Table 2 − Number of elements used and display component data of a 6,000 nits display

ELEMENT NUMBER	LCD TEMPERATURE (°C)	LED TEMPERATURE (°C)	OPTICAL GAP AIR SPEED (M/S)	OPTICAL GAP AIR PRESSURE (PA)
3,768,435	55.1	41.6	1.36	-0.2
4,321,359	54.6	41.6	1.36	-0.1
6,987,321	53.7	39.4	1.58	-16.8
7,801,800	53.2	38.3	1.65	-22.9
9,383,551	53.0	37.9	1.70	-29.1
11,270,681	52.9	37.8	1.73	-31.0
13,705,116	52.9	37.9	1.75	-33.8

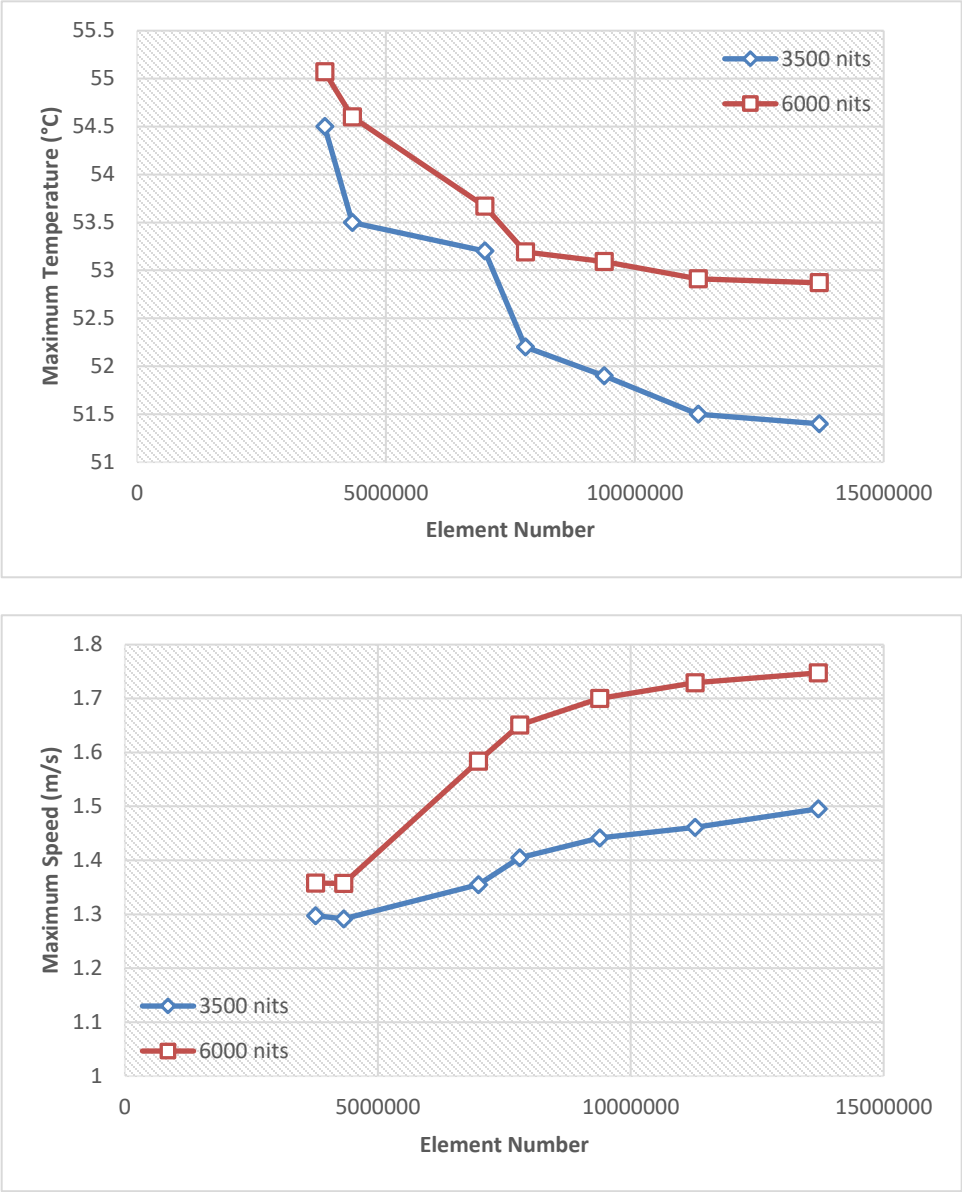

Figure 19 – Number of elements used and the maximum LCD temperature and optical gap air speed of 3,500 nits and 6,000 nits 55" displays

size, the overall temperature appears to have similar pattern, as the increase or decrease in value takes place in every point consistently. From Figure 20 which shows the LCD contour using 7.8 million elements and examining the temperature at the location of the thermocouples, it is shown that decrease in temperature is the largest at L1 and L4 where the difference in temperature was the highest between the simulation and experiment before the mesh refinement (see Table 3). The use of finer grid size gave out a better result that matches with the experiment.

4.4 Meshing technique effect

The effect of non-conforming and conforming mesh is examined as the use of non-conforming mesh allows huge reduction in element numbers and faster computational process, but due to possible incompatibility in shape functions that are used to numerically approximate governing equations in non-conforming boundaries, the use of non-conforming technique may yield a different result when compared to the use of conforming mesh [26]. The same domain and setup used for grid size study is re-meshed with 14.1 million elements to ensure a correct representation of solid parts after the mesh. The results are compared with that of the non-conforming mesh with 4.3 million elements as the element allocation in fluid region resembled the closest out of all non-conforming models. The overall temperature rises up to 1.16 °C for 6,000 nits display in the sun-sided components in the case of conforming mesh (see Table 4). The use of non-conforming mesh for a transition to thin parts results in underestimation of maximum temperature yet the difference is considerably small and consistently within small difference range for all components. For the simulation setup and computation

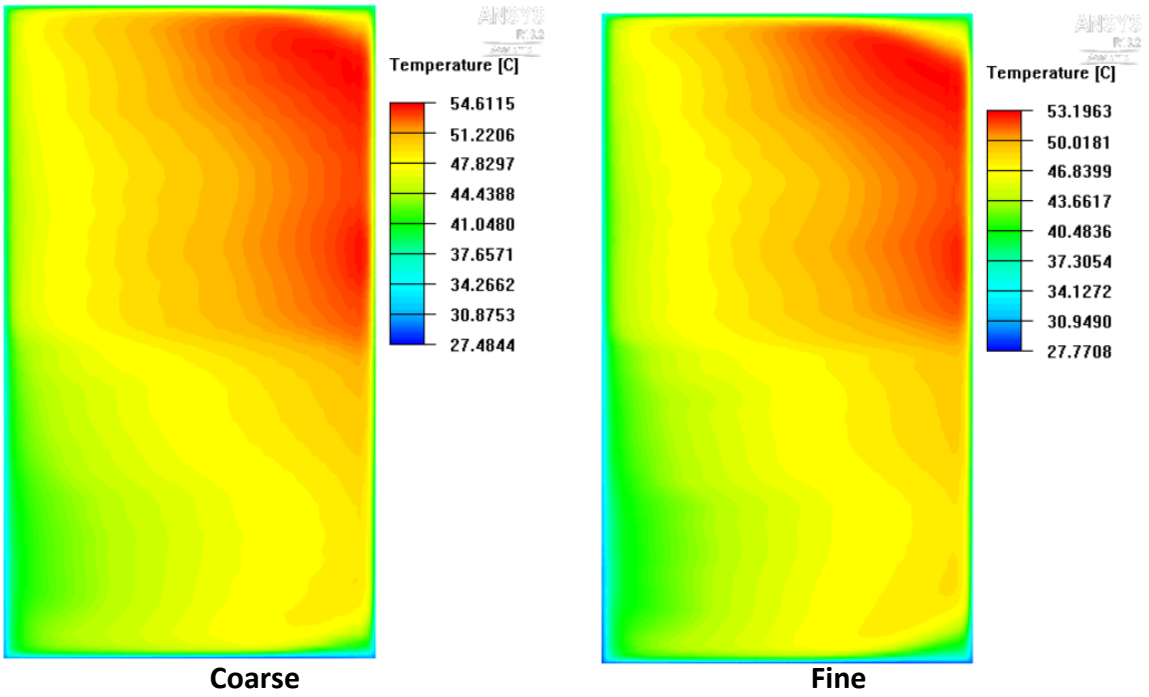

Figure 20 – LCD temperature contours from coarse (4.3 million) and fine (7.8 million) mesh settings

time, conforming mesh results in inevitable increase in element number due to extension of grid lines across the entire fluid domain and additional refinement to improve the aspect ratio of the elements for better convergence.

4.5 Simulation package comparison

For further validation, the same simulation under the worst outdoor condition is carried out using FloEFD. The temperature contour plots of the LCD and LED tiles for ICEPAK and FloEFD simulation for 3,500 nits display are displayed in Figure 21. For FloEFD, the maximum temperature on the LCD and LED tiles turn out to be 100.7°C and 76.1°C, respectively. Comparing the value to that of ICEPAK, at the coarse mesh setting, the maximum temperatures of the LCD and LED tiles are 103.1 °C and 77.1°C. ICEPAK gives out a more conservative result but comparing the overall temperature distribution, it

Table 3 − Grid size effect on the relative LCD temperature of a 6,000 nits display

	TEMPERATURE (°C)					
	L1	**L2**	**L3**	**L4**	**L5**	**L6**
EXPERIMENT	25.1	N/A*	35.7	25.6	33.9	40.3
COARSE MESH SETTING						
SIMULATION	31.7	N/A	42.2	31.6	38.4	42.9
DIFFERENCE	6.6	N/A	6.5	6.0	4.5	2.6
FINE MESH SETTING						
SIMULATION	30.0	N/A	39.1	29.8	37.0	42.3
DIFFERENCE	4.9	N/A	3.4	4.2	3.1	2.0

*Temperature data at L2 is unavailable due to the overwrite with the ambient probe data

Table 4 − Mesh technique effect on the component temperatures of a 6,000 nits display

	MAXIMUM TEMPERATURE (°C)		
	Non-conforming	**Conforming**	**Difference**
SUN-SIDE			
LCD	54.61	54.89	0.28
LED	41.61	41.92	0.31
BACKLIGHT	54.95	56.11	1.16
COOL-SIDE			
LCD	36.46	36.51	0.05
LED	35.30	35.80	0.50
BACKLIGHT	49.12	50.01	0.89

is observed that the maximum temperature is located in the middle left portion of LCD and LED tiles for both of the simulation results. With the use of finer mesh in ICEPAK, the maximum temperature decreases down to 100.8 °C and 75.8 °C for the LCD and LED and the difference between the two simulation packages appeared minimal. The temperature distribution matches closely between the two simulation packages.

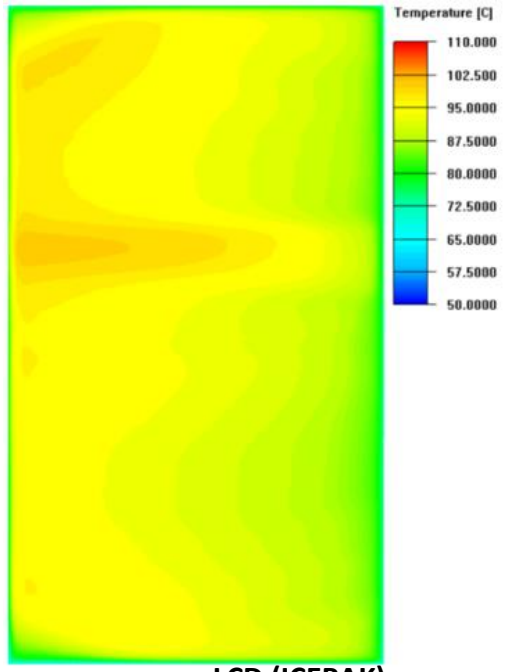

LCD (ICEPAK)

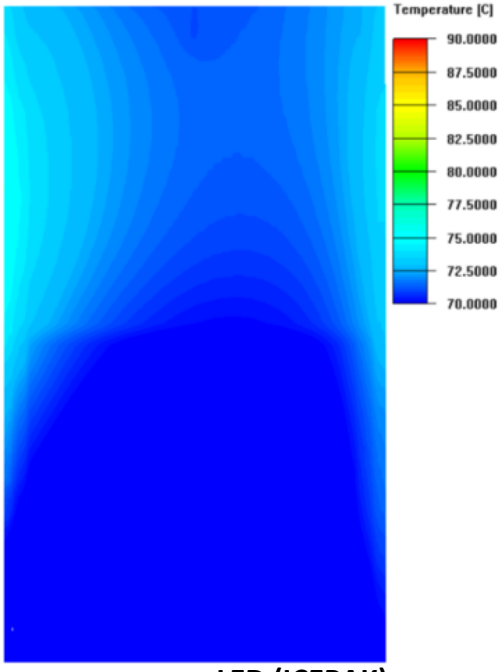

LED (ICEPAK)

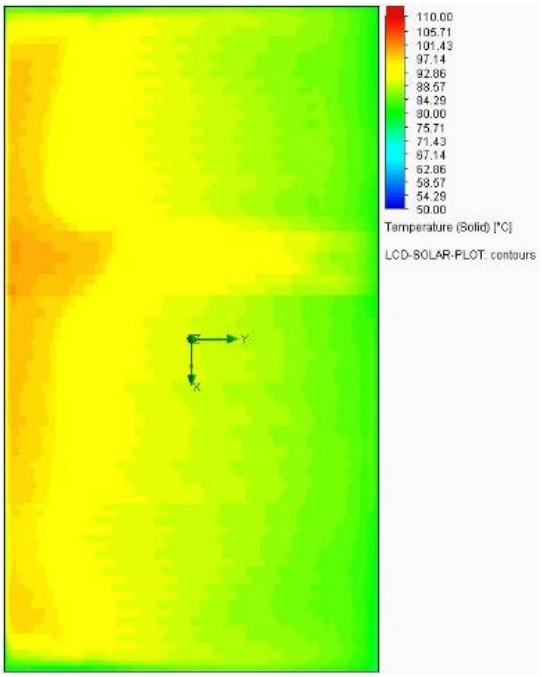

LCD (FloEFD)

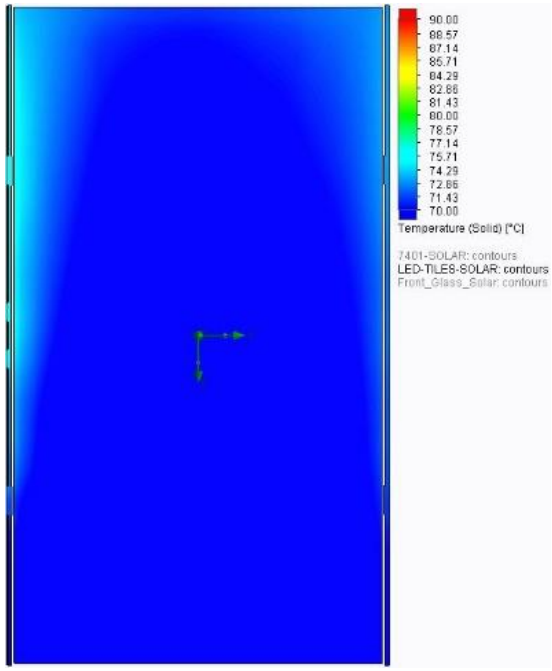

LED (FloEFD)

Figure 21 – LCD and LED temperature contours of 3,500 nits 55" display under the worst outdoor setting using different simulation packages

CHAPTER 5. SIMULATION IMPROVEMENTS USING BEER'S LAW AND GAP ADJUSTMENT EFFECT ON THE LCD

Based on the discussion in Chapter 4, the simulation results showed higher temperatures than the experimental results in the LCD. Such outcome allows the simulation result to be used as a conservative measure for thermal design of the product but even when mesh count is high enough to guarantee a grid independence of the simulation, the error between the two remains around 2 °C to 5 °C throughout the LCD surface. One of the key aspects that could be reconsidered to minimize such error resides in the heat distribution in the vandal glass which is heavily affected by the solar irradiance. The initial simulation done on the outdoor digital displays assumes that the solar irradiance on the semi-transparent vandal glass assembly is distributed evenly in each layer of glass. In this Chapter, in lieu of even heat distribution along the vandal glass, the resulting heat is reallocated in a way to provide more accurate and realistic simulation results. In addition, using the simulation tool, the closed-loop gap dimension is adjusted to see how the outdoor digital display can benefit from this parameter.

5.1 Vandal glass radiative properties testing

To better understand how the vandal glass interacts with the incident solar irradiance, a separate testing is conducted on a sample of the vandal glass. Spectral radiative properties of the glass in the visible and near-infrared region are measured using a monochromator a tungsten-halogen lamp and an integrating sphere [27], from 0.38 μm to 1.8 μm. The inner surface of the integrating sphere is coated with diffuse PTFE to

produce highly diffuse reflectance. Designed for measurement of diffusely reflecting surfaces, the integrating sphere can be used on smooth surfaces like the glass samples with proper modifications. A tilted sample holder is used to mount the samples to the integrating sphere to prevent the loss of the specular reflectance from the entrance port. In the transmittance measurement, the samples are placed at a fixed distance from the entrance port to avoid the multiple reflections at the inner surface of the samples. A Si and a Ge detector are used to cover the wavelength shorter and longer than 1 μm, respectively. The spectral measurements were performed at an increment of 10 nm and averaged over 10 data points at each wavelength to reduce the uncertainty. Due to the weaker signal from the tungsten lamp and lower sensitivity of the Si detector, the uncertainty is higher towards shorter wavelengths, especially in the ultraviolet region where $\lambda < 0.4$ μm. For the measurement in the near- to mid-infrared range from 1 μm to 20 μm, an ABB FTLA 2000 Fourier Transform Infrared Spectrometer (FTIR) is used, along with a deuterated triglycine sulfate detector. Measurements were taken with a resolution of 4 cm-1 and averaged over 64 scans to improve the signal-to-noise ratio. A specular accessory with an incident angle of 10° is used for reflectance measurement, and a gold mirror is used as the reference, with a reflectance of 0.985 based on its optical constants [28]. The specular transmittance was also measured at normal incidence using FTIR. In the overlapped region from 1 μm to 1.8 μm, reflectance and transmittance measurement from both FTIR and the monochromator show high consistency. The specifications for the apparatus used in the radiative properties testing is listed in Appendix A. The testing was conducted in Atlanta, GA in April 2019. The obtained spectral radiative properties of the vandal glass are plotted in Figure 22.

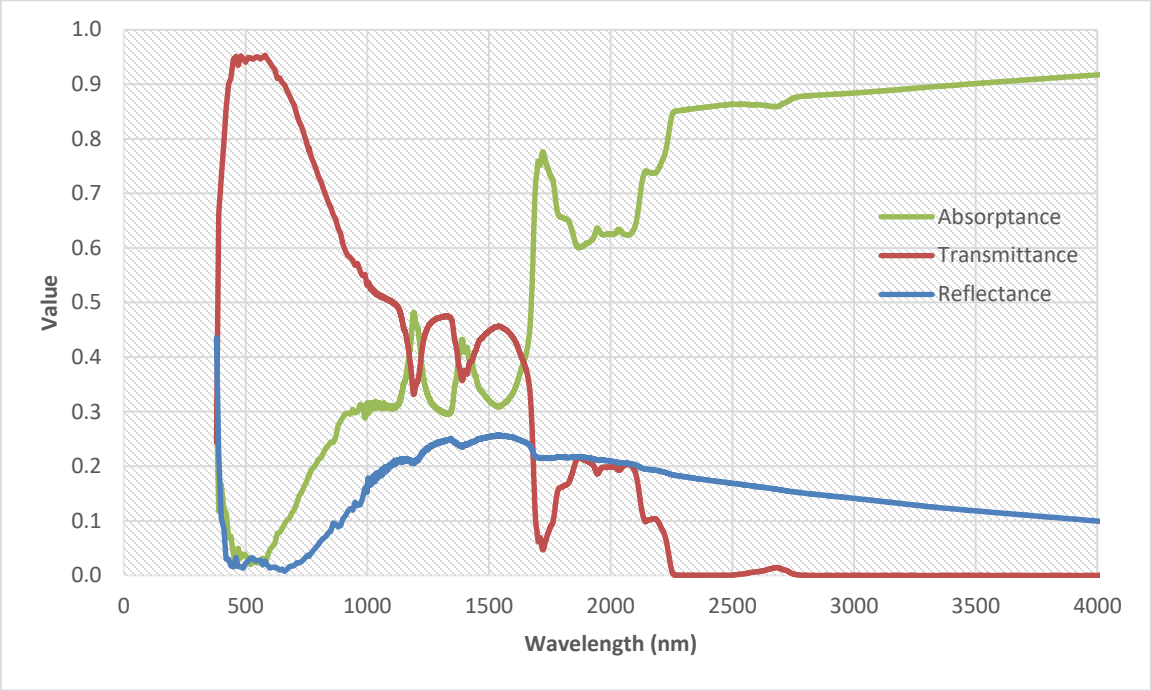

Figure 22 – Spectral radiative properties of the vandal glass

5.2 Heat load reallocation in the vandal glass

Initially, a new approach to find out how much heat load should be allocated in each layer of glass involved a simulation setup of a 2-dimensional domain of the glass assembly and numerically solving the radiative heat transfer equation using the following Discrete Ordinates (DO) method:

$$\nabla \cdot (I_\lambda(r,s)s) + (a_\lambda + \sigma_s)I_\lambda(r,s) = a_\lambda n^2 I_{b\lambda} + \frac{\sigma_s}{4\pi}\int_0^{4\pi} I_\lambda(r,s')\Phi(s\cdot s')d\Omega' \qquad (2)$$

Yet, the use of DO method did not seem feasible due to several factors:

1) Each layer of glass assembly is joined by an adhesive to minimize any reflection within the assembly and to guarantee the highest visibility through the multiple layer of glass. Assuming the reflectance occurs at a surface level, not throughout the volume like absorption and transmittance, a valid radiative

property of the adhesive could not be obtained due to the different surface finishing and roughness when an individual layer is tested.

2) The values of scattering coefficient, σ_s, and the phase function, Φ, for the set of glass were not obtainable. Thus, a different approach to the problem was used.

Given that the values of incident solar intensity and the transmitted solar intensity can be obtained, an approximation for the intensity decay can be made using Beer's law [29]:

$$\frac{I_{\lambda,t}}{I_{\lambda,0}} = \mathrm{e}^{-a_\lambda t} \tag{3}$$

which states that the spectral intensity decreases exponentially in response to the penetration depth. A similar correlation can be found for an absorbing nonmagnetic medium with an electromagnetic wave incident on the surface [30]:

$$\langle S \rangle = \frac{n}{2\mu_0 c_0} E^2 \mathrm{e}^{-a_\lambda t} \tag{4}$$

$$a_\lambda = \frac{4\pi\kappa}{\lambda} \tag{5}$$

which shows that the amplitude of the energy flux, *S*, in the direction of *t* decays exponentially according to $\mathrm{e}^{-a_\lambda t}$.

Based on this idea and using a solar irradiance spectrum at sea level at Air Mass 1.5 (a zenith angle of 48.2°) from National Renewable Energy Laboratory as shown in Figure 23 [31], of the initial amount of solar spectra projecting onto the glass assembly, the spectral irradiance after a reflection can be calculated using:

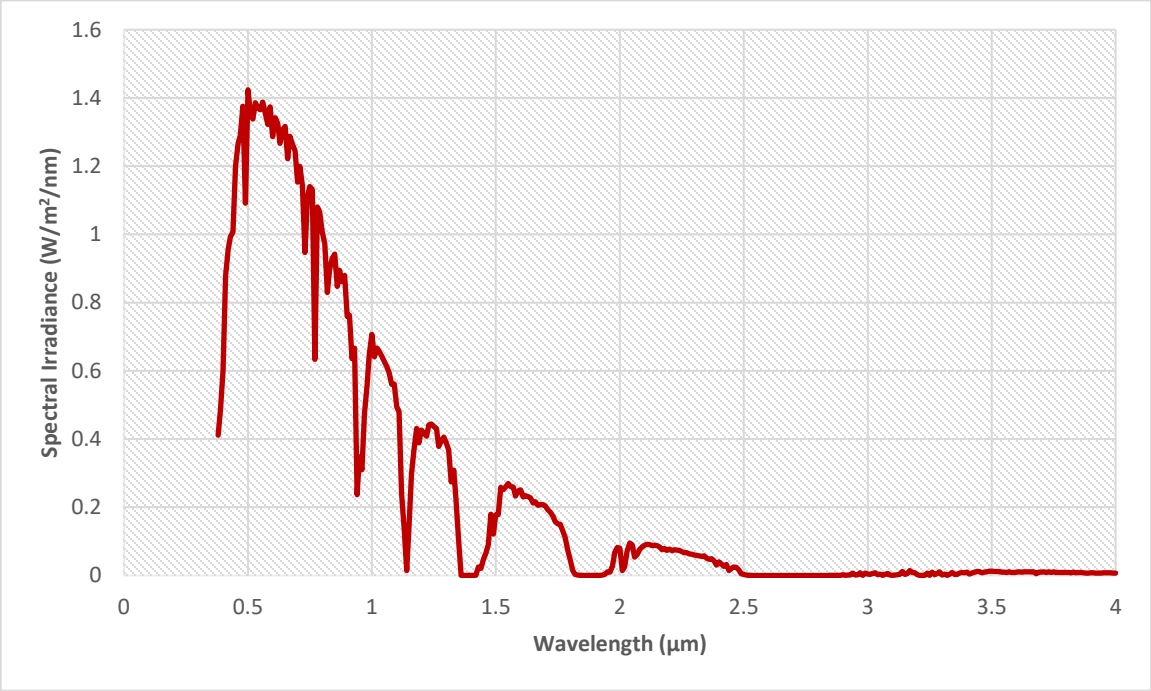

Figure 23 – Spectral solar irradiance at sea level at Air Mass 1.5

$$G_{\lambda,0} = G_{\lambda,i} \cdot (\alpha_\lambda + \tau_\lambda) \tag{6}$$

Subsequently using Eq. (3) and (6), the absorption coefficient, a_λ, can be obtained which then, is plugged back into Eq. (3) to see how much spectral irradiance gets absorbed at a different thickness:

$$G_{\lambda,a} = G_{\lambda,t_2} - G_{\lambda,t_1} \tag{7}$$

The spectral values are then converted into the overall values by taking the integral over the wavelength:

$$G = \int G_\lambda d\lambda \tag{8}$$

In a similar manner as done for the true solar testing, the obtained irradiance values are used to calculate the absorption factor and the heat load, using Eq. (2).

5.3 Heat load reallocation and improved simulation results

Unlike the initial simulation where the heat load in the vandal glass, obtained from the true solar testing, was assumed to be evenly distributed in each layer of glass, the heat load on the vandal glass follows the methodology defined by the exponential decay of heat where the highest amount of heat load is assigned to the first glass layer and smaller amount on the subsequent glass layer away from the incident solar irradiance for the new simulation on a 6,000 nits display.

Of the obtained properties in the domain of 380 nm to 20,000 nm, the values within the global shortwave radiation were considered for this research: 380 nm to 4,000 nm. Multiplying the spectral irradiance, $I_{\lambda,i}$, with the spectral absorptance, transmittance and reflectance, the solar irradiance is decomposed into absorbed, transmitted and reflected components in response to the contact with the glass assembly (see Figure 24). The decomposed spectral irradiance is then plugged into Eq. (3) and (6) to get the absorption coefficient, a_λ, shown in Figure 25. Following Beer's law at the spectral level and taking the integration over the wavelength, using Eq. (5.7), of 887.8 W/m^2 solar irradiance that is projected perpendicular to the glass assembly, 82.8 W/m^2 (9.3%) is reflected and 183.8 W/m^2 (20.7%) is absorbed indicating that the remaining 621.2 W/m^2 (70.0%) is transmitted. Comparing this value to the result from true solar testing where the ratio of transmitted solar irradiance to the initial solar irradiance was found out to be around 75.7%, similar to the transmission percentage obtained using Beer's law (see Table 5). 183.8 W/m^2 of the absorbed solar irradiance is then re-allocated in each layer of glass and adhesive at the spectral level using Eq. (5.6). Taking the integral of the value over the same wavelength domain as done prior, it is found out that 110.9 W/m^2 (12.5%)

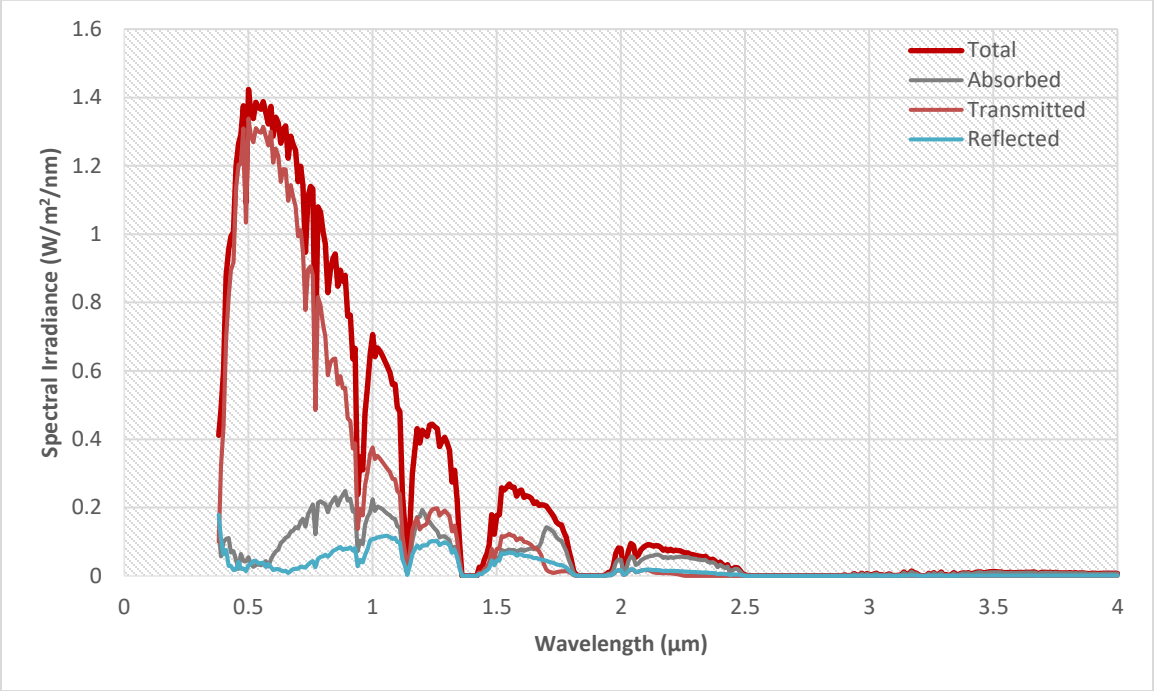

Figure 24 – Decomposed spectral solar irradiance in response to the vandal glass

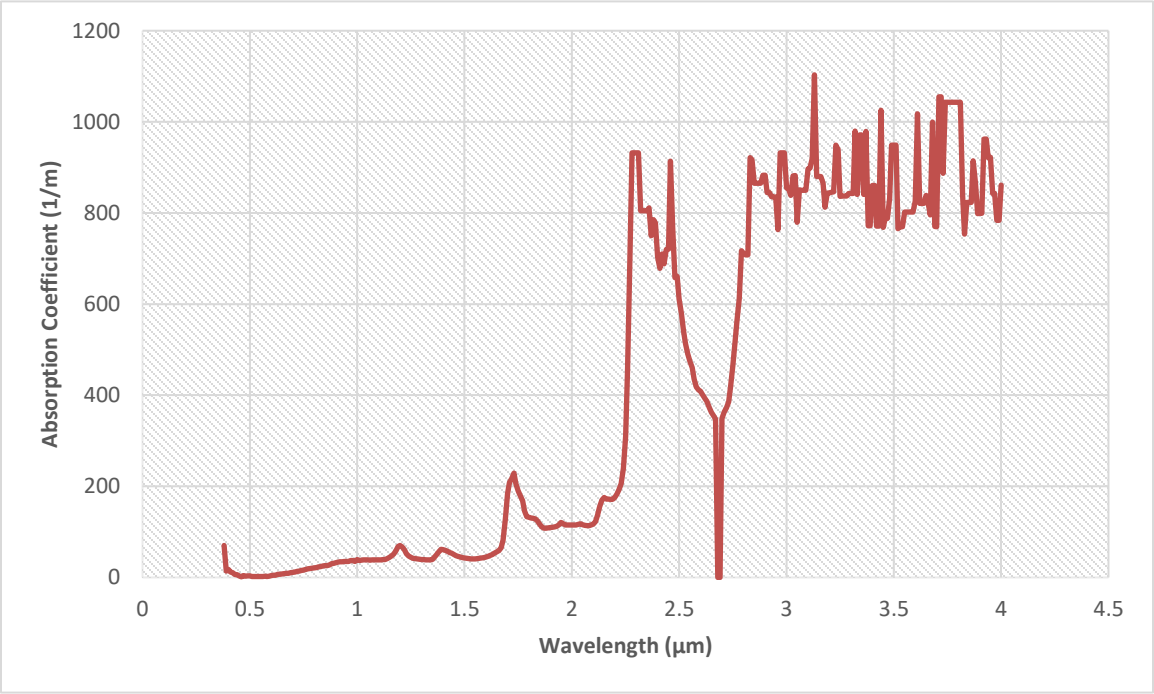

Figure 25 – Absorption coefficient of the vandal glass

Table 5 − True solar testing results on the vandal glass

TRIAL	IRRADIANCE (W/M^2)		
	Initial	**After**	**Transmitted (%)**
1	825	618	74.9
2	828	626	75.6
3	824	623	75.6
4	829	630	76.0
5	827	629	76.1
6	827	628	75.9
7	836	638	76.3
8	836	637	76.2
9	839	625	74.5
	Average		
	830	628	75.7

of irradiance gets absorbed by the front glass where the percentage value in parenthesis represents the absorption factor, η. Similarly, 18.6 (2.1), 13.7 (1.5), 16.5 (1.9) and 24.0 W/m^2 (2.7%) of irradiance is absorbed by the first adhesive, touch glass, second adhesive and rear glass, respectively (see Figure 26).

Two separate simulations are performed under the ambient temperature of 10.5 ℃ and the solar irradiance of 800 W/m^2. For each simulation, all mesh settings and power settings were kept the same besides the heat load on the glass assembly and the LCD. The original simulation assumed even distribution of heat load among the glass components whereas the new simulation assumed heat distribution as calculated using Beer's law; the remaining irradiance that is transmitted through the last layer of the glass is assumed to be entirely absorbed by the LCD. The LCD temperature contour of the new simulation is displayed in Figure 27. The general heat distribution along the LCD cell remains the same as that of the original simulation where a hotspot is observed in upper right side of the cell and the heat dissipates through the left side. Five thermocouples are placed on the LCD to compare the temperature value of the original simulation and the experiment [6]. The new simulation data are added and compared to the values (see Table 6). Using the Beer's law model, the data mismatch between the simulation and the experiment reduces at all five thermocouple locations as low as 0.8 ℃ to as high as 1.7 ℃. The difference remains relatively high at the left side of the LCD but at the location of the hotspot, the difference is observed to be as low as 1.0 ℃.

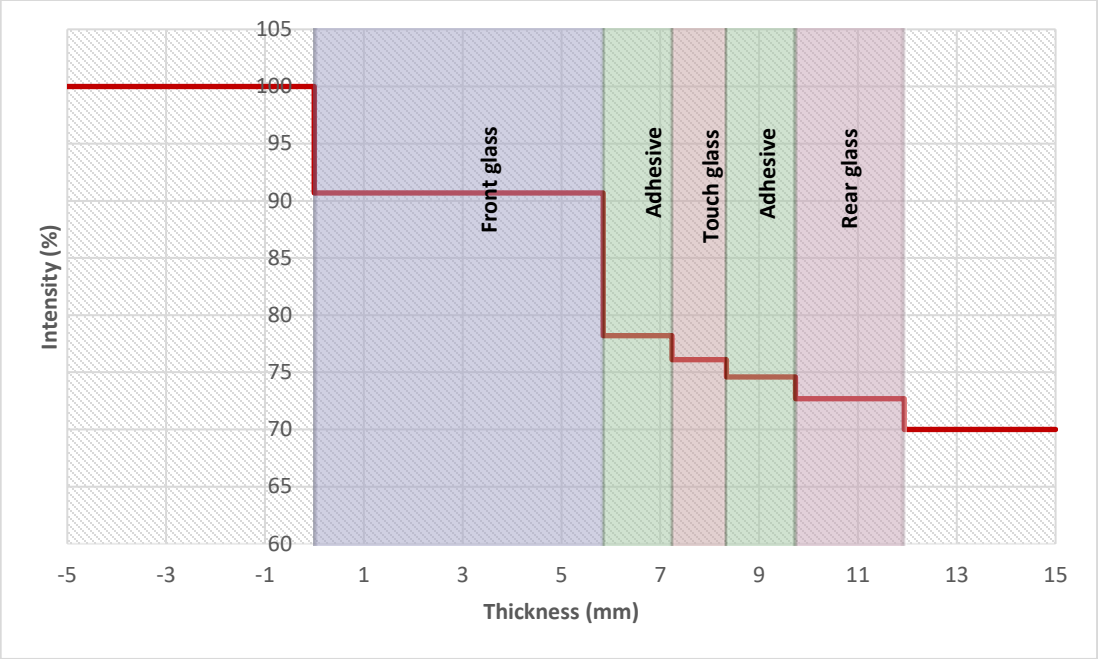

Figure 26 – Variation in solar irradiance through the vandal glass

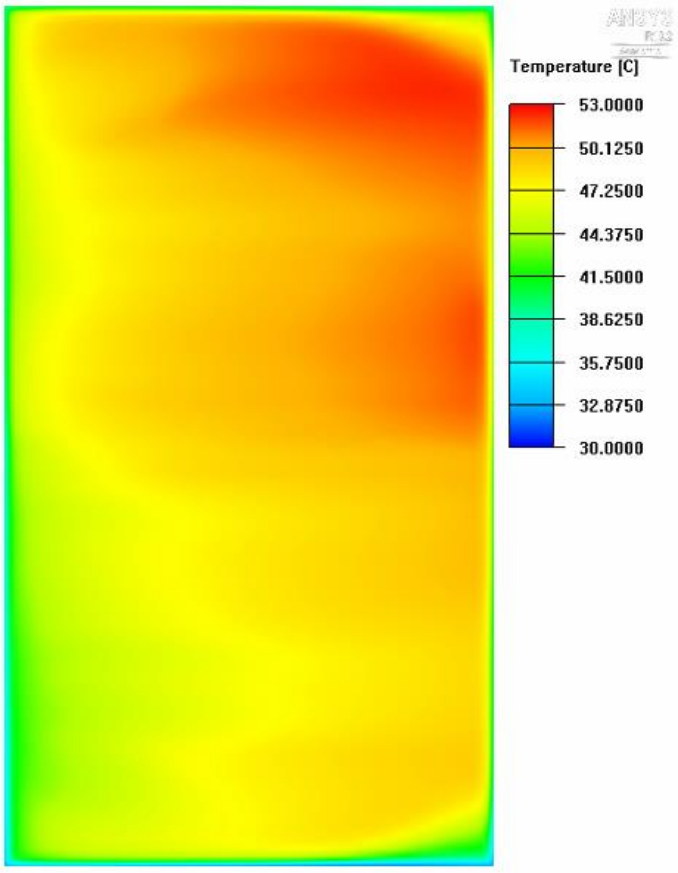

Figure 27 – LCD temperature contour using Beer's law approximation

Table 6 − LCD temperature comparison using Beer's law approximation

	TEMPERATURE (°C)					
	L1	**L2**	**L3**	**L4**	**L5**	**L6**
EXPERIMENT	35.6	N/A*	46.2	36.1	44.4	50.8
SIMULATION (INITIAL)	40.5	N/A	49.6	40.3	47.5	52.8
DIFFERENCE (INITIAL)	4.9	N/A	3.4	4.2	3.1	2.0
SIMULATION (NEW)	39.7	N/A	47.9	39.6	47.4	51.8
DIFFERENCE (NEW)	4.1	N/A	1.7	3.5	3.0	1.0

*Temperature data at L2 is unavailable due to the overwrite with the ambient probe data

5.4 Closed-loop gap adjustment effect

For the parametric study, additional simulations are performed where the heat load is assumed to be evenly distributed as done in the original simulation but the air gap between the LCD and the glass assembly is adjusted. It has been shown that for this particular simulation on a 6,000 nits display, 7.8 million elements with a minimum of 5 elements kept in the fluid gap are necessary to achieve a grid independence thus about 7.9 to 8.1 million elements are used for all simulations where a minor variation in the element number is due to the effect of gap adjustments.

The fan performance curve for the closed-loop fan is shown in Figure 28. As the increase in pressure rise typically results in undesirable side-effects such as high noise and reduced flow rate which amplifies significantly within the stall region, represented by a near-zero slope at around 260 Pa pressure-rise, the operating points of three closed-loop

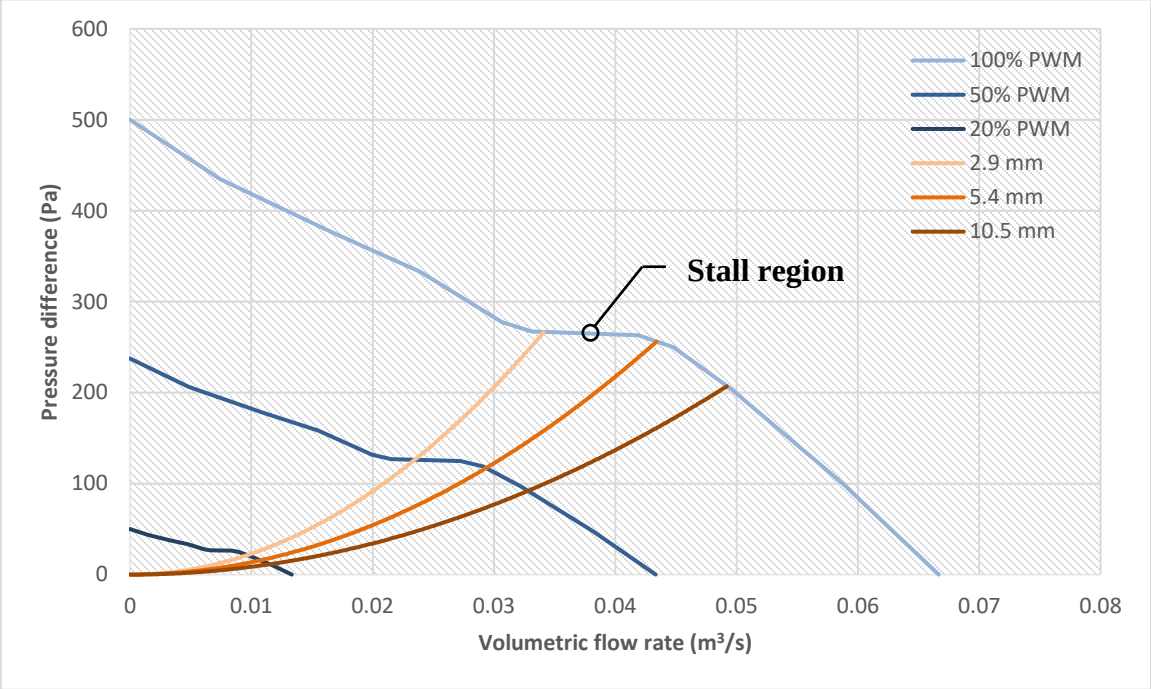

Figure 28 – Closed-loop fan system and performance curve

fans located in the chassis need to be monitored so they are on the right half of the performance curve after the gap adjustment. From the post-processing, it is shown that the closed-loop fan located in the center experiences the highest pressure rise for all cases and the further analysis focuses on this particular closed-loop fan. Figure 29 shows the pressure rise and volumetric flow rate of the closed-loop fan for the gap adjustments from5.4 mm to 10.5 mm. Both data sets show a plain correlation between the gap distance and the fan performance with no obvious outliers where 97% of the pressure rise data points could be explained by a linear relationship and 94% of the volumetric flow rate data points could be explained by a linear trend. The fan system curves for the gap adjustments at 2.9, 5.4 and 10.5 mm are overlaid in Figure 28 using the below equation [32]:

$$\Delta P = K \cdot q^2 \tag{9}$$

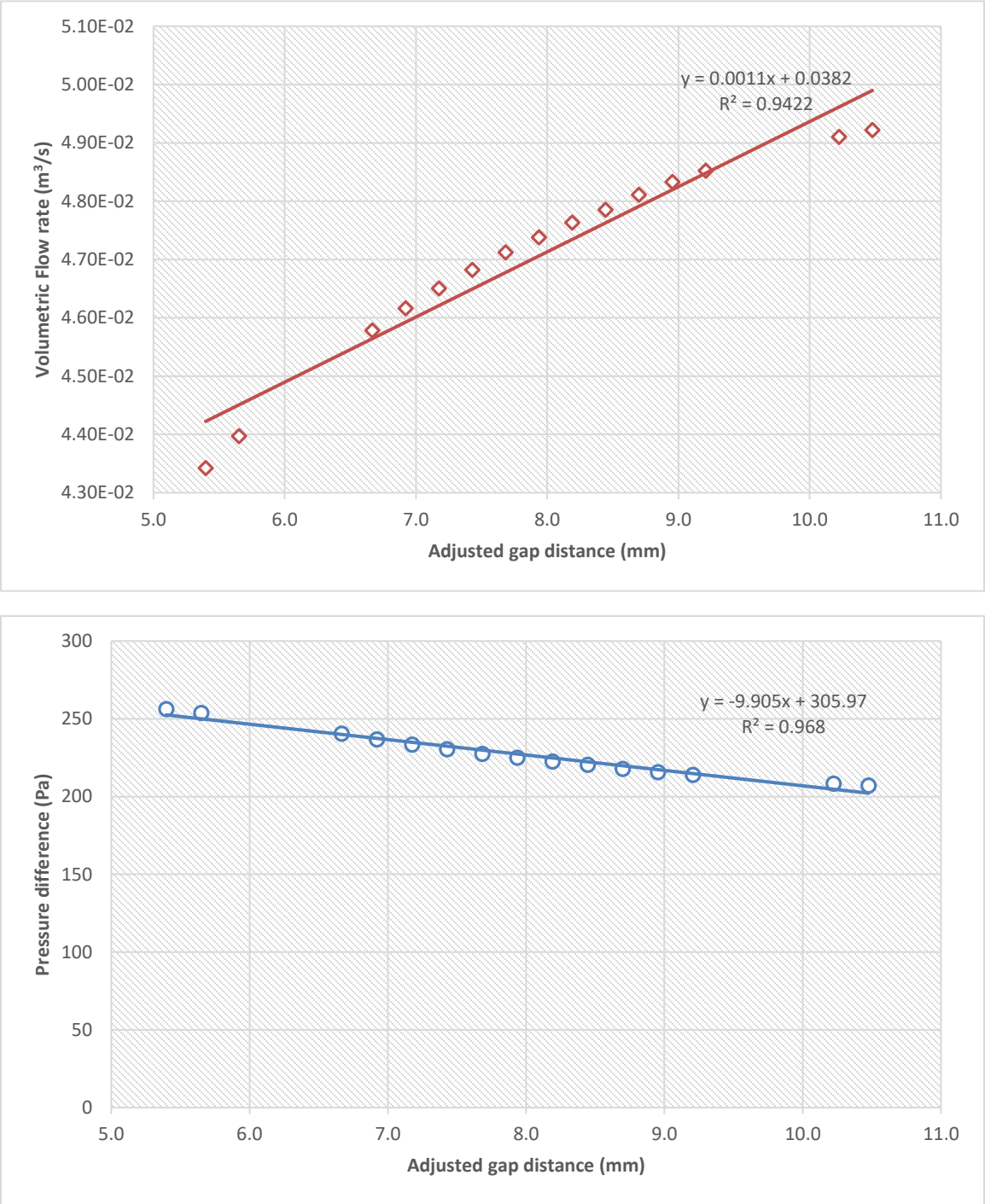

Figure 29 – Gap effect on flow rate and pressure-rise of the closed-loop fan

Based on the linear trend as observed in Figure 29, the fan performance improves with better flow rate as the gap distance increases. At 2.9 mm gap distance, the fan operates in the stall region which has a sudden decrease in volumetric flow relative to the change in pressure rise. To summarize, the fan performance can be improved as the gap increases and as long as the gap stays larger than 5.4 mm, the operating point is inside the safe operating region and the fan performance is of no concern. The gap effect on the LCD temperature and how the closed-loop fan contributes to the cooling effect are examined next.

The variation in LCD maximum temperature depending on the gap distance between the LCD and the glass assembly is plotted in Figure 30. Total of 16 simulations are conducted where the original gap is set at 7.9 mm (0.3125”), marked as a filled point, apart from each other. additional simulations are displaced in the scale of 0.254 mm (0.01”) apart from the initial placement, both inward and outward. Without any gap adjustments, the LCD maximum temperature under the ambient temperature of 50 °C and solar irradiance of 1,250 W/m^2 turns out to be 104.4 °C. Within the 6.7 mm to 9.2 mm gap range, a deviation in temperature from the original value stays relatively small, within ± 0.2 °C range. The decrease in gap resulted in reduction in LCD temperature as low as -0.1 °C at 7.2 mm but a further decrease in gap starts to have an adverse effect where the LCD temperature rapidly grows to 105.4 °C at 5.4 mm and 114 °C at 2.9 mm which is not shown in Figure 30.

As the decrease in gap distance have two contrasting flow effects, where the volumetric flow rate of the closed-loop fans reduces and the cross-sectional area of the closed-loop passage between the LCD and the glass assembly decreases, the gap effect on

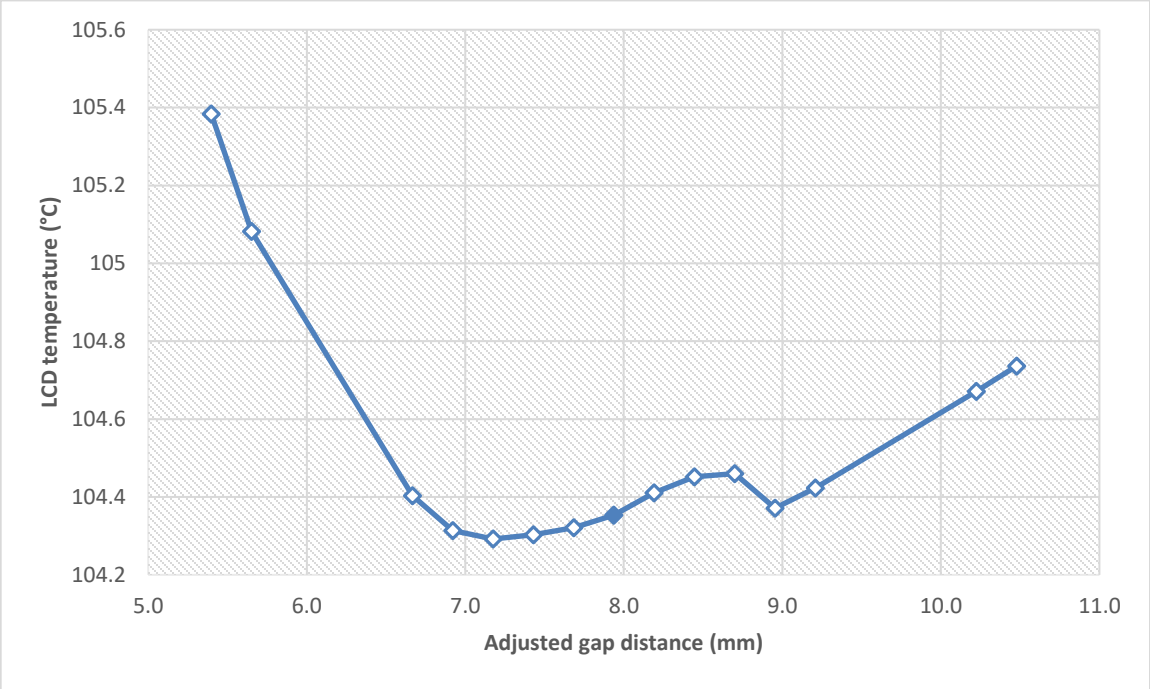

Figure 30 – Gap effect on the LCD maximum temperature

the LCD temperature is assumed to be a balance between the fan performance and the dimension of the flow region. From the fan performance analysis, for the gap adjustments from 5.4 to 10.5 mm, the volumetric flow rate to the gap distance ratio is 0.0011 $m^3/s/mm$ and other two closed-loop fans with higher flow rate shows a similar trend indicating that 0.254 mm (0.01") decrease in the gap can effectively reduce the overall flow rate inside the closed-loop passage by 0.0083 m^3/s. For the closed-loop passage between the LCD and the glass assembly, the gap adjustment resulted in 0.0031 m^2 cross-sectional area reduction where the same display components are placed on the opposite side of the chassis, resulting in a total of 0.0062 m^2 reduction in the passage area, indicating the fan performance has greater impact in overall air speed in the closed-loop passage. From the CFD/HT analysis, it shows that for the gap adjustments at 6.7 mm and less, such assessment remains true and the average air speed reduces down to below 4.82 m/s

whereas the air speed is determined to be 5.07 m/s for the original gap. For the gap adjustment at 7.2 mm which gives the lowest LCD maximum temperature of all, the opposite behavior is observed where the average air speed increases to 5.11 m/s and starts to decrease as the gap distance increases further. The average temperature of the LCD follows the same trend as the average air speed in the closed-loop passage where the value consistently increases as the gap distance increases, reaching from 96.7 °C at 5.4 mm to 97.5 °C at 10.5 mm with an exception at the local minima observed at 6.7 mm with an average temperature of 96.1 °C.

It is observed that the increase in gap results in a consistent, although small, decrease in LED temperature and an increase in the cavity air speed. Overall, the thermal effect of gap adjustments is not as prominent due to the fact that the closed-loop air can divide into either passage at the cavity and the gap. As long as the gap stays between 6.7 to 9.0 mm range, the LCD does not experience any significant increase in maximum temperature and this parameter can be reconciled with the desired fan performance.

CHAPTER 6. DISPLAY DEFLECTION AND SIMULATION RESULTS ON A 98” OUTDOOR DIGITAL DISPLAY

In this chapter, using the simulation setup as done for the 55” outdoor digital displays, a simulation on a 98” outdoor digital display under 3,500 nits brightness output is performed.

6.1 Screen bending effect and simulation setup modifications

Due to the body force and pressure difference inside the unit, it is seen that the LCD experiences a deflection that is measured to be 2 mm or higher in the center depending on the screen size. For the simulation done on 55” outdoor digital displays, every component is assumed to be flat but given that the closed-loop air passage between the LCD and vandal glass is less than 10 mm and the observed deflection is in a scale of millimeters, the reduction in flow area cannot be ignored and is likely to have a non-negligible effect on the flow behavior and the LCD temperature. In a 98” outdoor digital display simulation, the bending effect on the LCD is artificially taken into account by modifying the geometry and a 6 mm deflection in the center of the LCD is made. For the domain boundary, since open-loop fans are placed on the bottom of the unit for this case in which the air enters the unit from the top and leaves to the bottom, a pressure inlet and outlet are assigned on top and bottom surface of the domain, respectively. Due to a larger screen size, the heat load due to the solar irradiance has been recalculated and listed in Table 7. On the LED tiles, as done for the 55” outdoor digital

Table 7 − Heat loads due to the solar irradiance on a 98” display

PART NAME	ABSORPTION FACTOR	AREA (M^2)	IRRADIANCE (W/M^2)	HEAT LOAD (W)
GLASS MASK	0.79	0.498	1,250	492
VANDAL GLASS	0.26	2.625	1,250	853
LCD	1.00	2.625	925	2,461

displays, 70% (1,605 W) of the input power is assigned and the remaining 30% (688 W) are assumed to be absorbed by the air in the optical gap.

6.2 Simulation results

The temperature contours on the LCD and LED are displayed in Figure 31 under the worst outdoor setting. Similar to the convective cooling taking higher impact near the air entrance region in the 55” units, a hotspot is observed in the lower right corner of the LCD and LED. In the 98” unit, the open-loop air enters from the top and exits to the bottom which explains why the upper half of the screen remains at lower temperature than the lower half. The maximum temperature reaches 105.7 °C and 85.0 °C in the LCD and LED, respectively. In the LCD, rather than a uniform region, multiple blotches of hotspot are observed which is largely due to the meshing mechanism behind ICEPAK software: subsequently observed in FloEFD.

With the use of hexa-dominant cartesian meshing, whenever an elevation due to a deflection is made, the outer element is open to an additional convective surface,

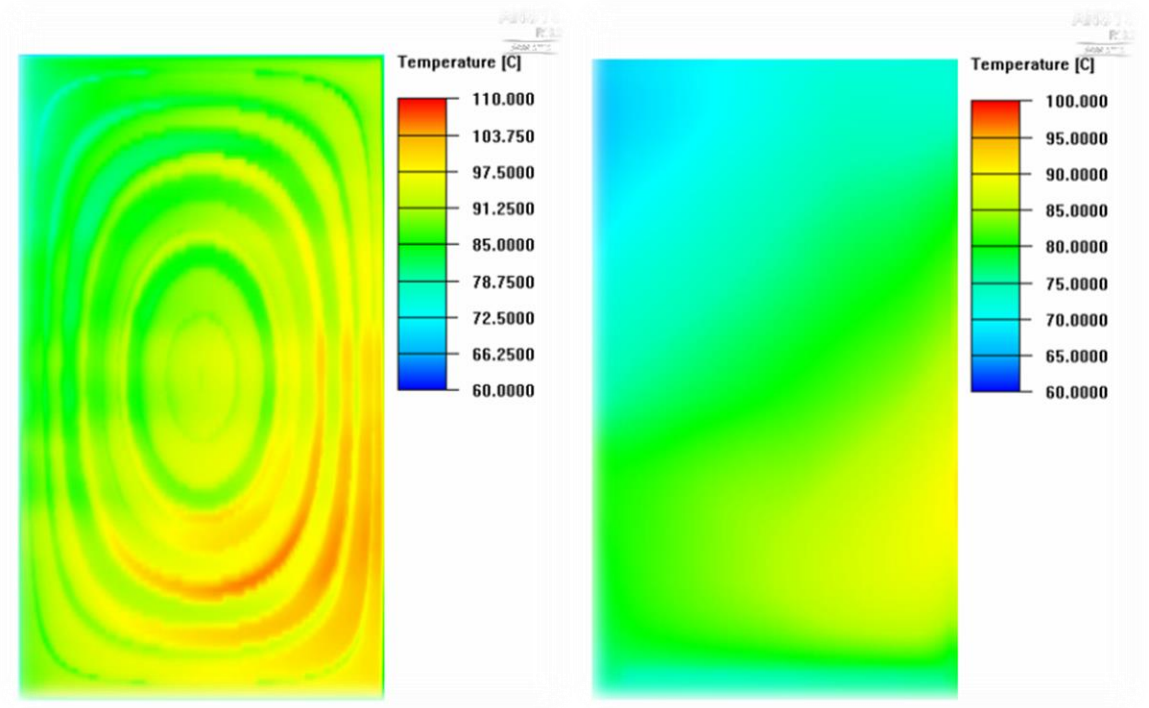

Figure 31 – Temperature contour of sun-sided 98” display components

experiencing an enhanced cooling effect. To observe how the artificial accountment of bending effect contributes to the pressure difference in the LCD, the cross-section pressure contour is shown in Figure 32. The bending effect is artificially accounted for in the simulation and noticing that the system pressure is lower in the cavity region compared to the air gap between the vandal glass and the LCD, it can be predicted that a peak deflection is likely to be present near the exit of the closed-loop air. The exact deflection throughout the LCD area is unknown but since the hotspot is present on the downstream of the deflection peak based on the pressure comparison in the 55” and 98” outdoor digital displays and given that the convective cooling effect weakens on 1 mm deflection and above, the LCD temperature near the hotspot could be slightly higher than it is in the initial simulation. The effect of solar irradiance, in comparison, would be lower than it is with the deflection considered since the reflectivity of most glass

increases as the incident angle increases and vice-versa for transmissivity [33]. With the above facts considered, a better result that resembles the experimental result could be obtained.

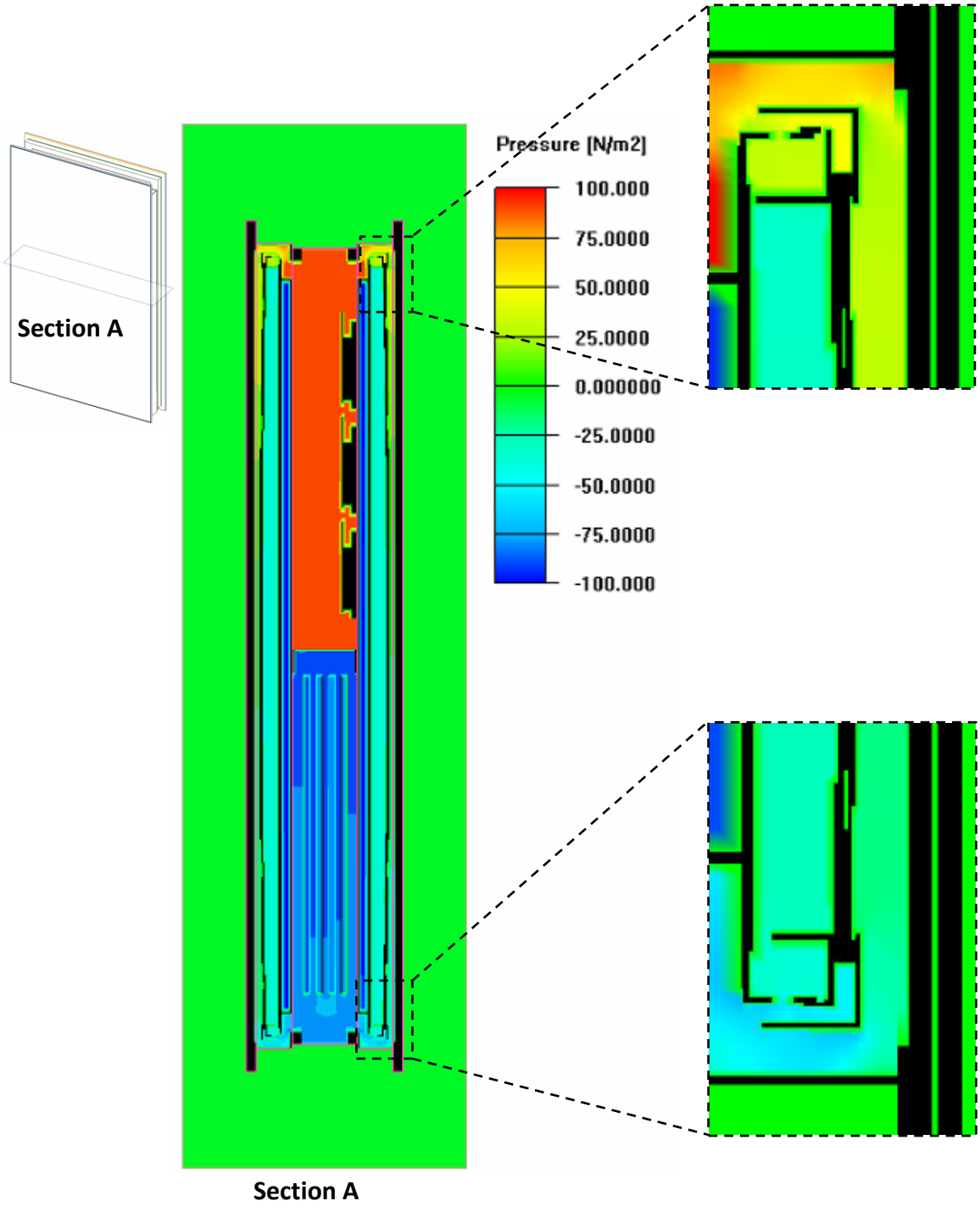

Figure 32 – Pressure contour of the closed-loop of the heat exchanger in the 98" display

CHAPTER 7. CONCLUSION AND FUTURE WORK

In this research, thermal modeling on outdoor digital displays is performed and validated by comparing the results of CFD/HT simulation and experiment. It has been shown that the simulation gives out higher temperature at all irradiance settings. While the temperature difference grows up to 6.6 °C on the cool side of the LCD surface as the solar irradiance increases, the overall temperature distribution and location of the hotspot from the simulation matched with the experimental data. Furthermore, the grid size study has shown that the difference between the two data set can be mitigated by using finer grid size. By using non-conforming mesh to reduce the number of elements and maintain good element quality CFD/HT software is able to give out good prediction on temperature limits of display components.

To better reduce the error, an attempt to make a modified CFD/HT model of outdoor digital displays is described in this research by assuming an exponential decay of the solar irradiance throughout the sun-sided vandal glass, in lieu of an even heating contribution from the solar spectra. In addition to the spectral absorption modeling, the gap distance between the LCD and vandal glass is adjusted to see how the system temperature and pressure could be affected. It has been shown that the exponential decay model better predicts the LCD temperature at all location. The gap adjustment has a growing adverse effect as the gap distance deviates further from 6.7 mm to 9.0 mm range where the maximum LCD temperature grows as high as 105.1 °C at ±2.2 mm away from the initial position and 105.4 to 114 °C at ±2.5 and 5.0 mm away. The air velocity with direct impact on the heat dissipation from the LEDs consistently increases as the gap

increased in the cavity opening. In the closed-loop passage located between the LCD and the glass assembly, a sudden increase in air speed was observed at 7.2 mm gap distance and the speed deemed hard to predict by just the correlation between the fan flow rate and the cross-sectional area of the passage. Regardless, within 6.7 to 9.0 mm range, the LCD temperature does not vary as much, and it is concluded that the optimal gap distance could be determined based on the desired fan performance which has a stronger impact on flow as the gap increased. While this gap study assumes the flexible LCD remains completely flat, it is observed that the LCD's shape becomes non-flat when it is affected by the air flow adjacent to it.

The deflection in the LCD is expected to be the highest near the hotspot where the highest pressure difference is observed. Given that the parametric study shows the maximum temperature of the LCD does not suffer much as long as the closed-loop gap stays within a certain range, the impact of solar irradiance on the optical films and LCD may require more thorough analysis as it is seen that the radiative properties tend to change depending on the incident angle of the solar irradiance. By coupling CFD/HT simulation results with mechanical simulation, the correct representation of screen bending can be found and its impact on the LCD temperature can be re-calculated. There are other sets of future work that can be done such as transient analysis and parametric study on other adjustable components, but thermomechanical analysis could be the key factor out of all of the possible options to further improve the current thermal modeling of outdoor digital displays.

APPENDIX A

EQUIPMENT SPECIFICATIONS

Self-Adhesive Thermocouples (SA3)

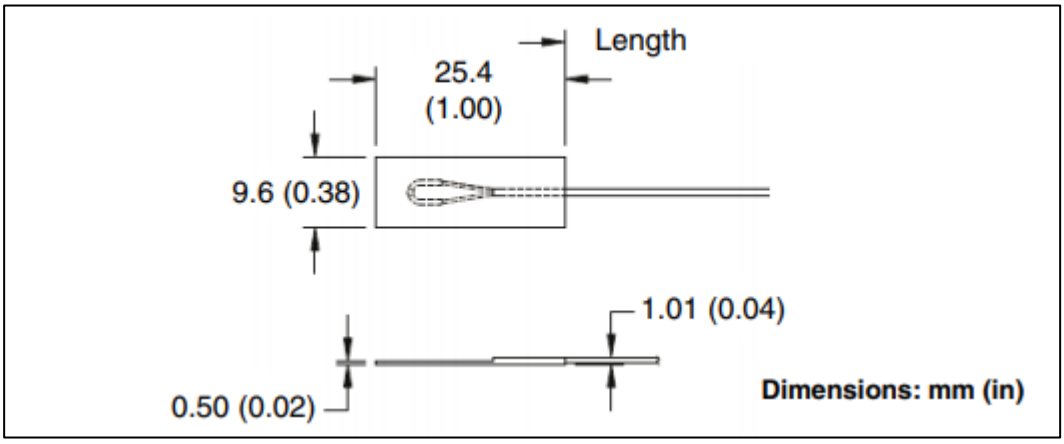

SA3 SPECIFICATIONS

ACCURACY		Special limits of error
JUNCTION TYPE	Ungrounded sensor construction	Polyimide tape base with silicone adhesive and paper peel sheet
		Polyimide tape cover
		PFA insulated and jacketed 30 AWG cable
		Glass filled nylon connector when specified
TEMPERATURE RANGE	Sensor	-17 to 260°C
	Connector	-29 to 180°C
INSULATOR RESISTANCE		100 MΩ minimum at 100 Vdc at room temperature and sensor mounted to surface

SP-420 Pyranometer

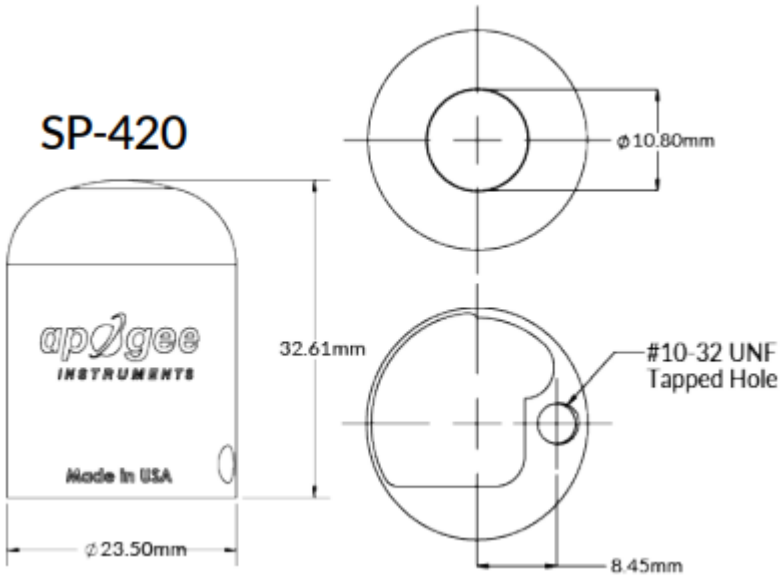

SP-420 SPECIFICATIONS

RESOLUTION	0.1 W/m^2
CALIBRATION UNCERTAINTY	5%
MEASUREMENT REPEATABILITY	<1%
NON-LINEARITY	<1%
SPECTRAL RANGE	280 to 4000 nm
DIRECTIONAL (COSINE) RESPONSE	± 5 % at 75° zenith angle
TEMPERATURE RESPONSE	0.04 ± 0.04 % per C
OPERATING ENVIRONMENT	-40 to 70 C
DIMENSIONS	24 mm diameter, 33 mm height

Cornerstone 130 Monochromator

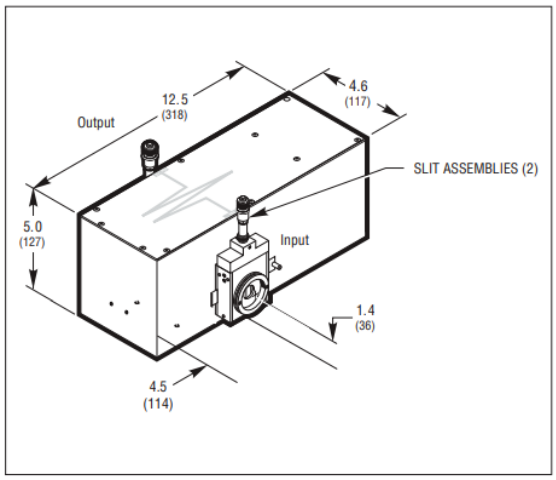

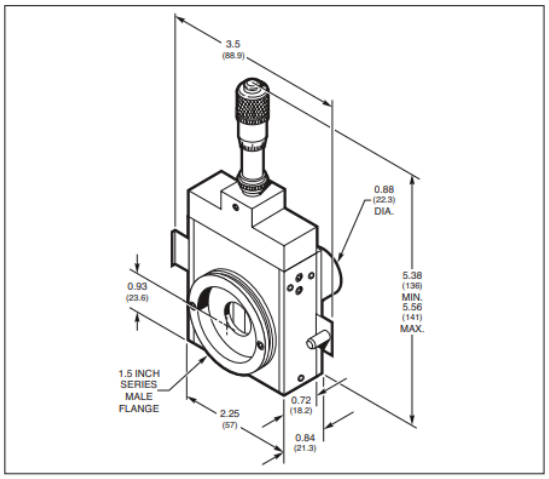

CORNERSTONE 130 SPECIFICATIONS

FOCAL LENGTH	130
WAVELENGTH SELECTION METHOD	Motorized
USABLE WAVELENGTH RANGE	180 to 2500 nm, grating dependent
SPECTRAL RESOLUTION	Grating and slit width dependent
WAVELENGTH ACCURACY	0.50 nm
WAVELENGTH PRECISION	0.11 nm
MAXIMUM SLEW RATE	350 nm/s with 1200 line/mm grating
STRAY LIGHT	0.03%
SHUTTER MINIMUM EXPOSURE TIME	0.2 s
SHUTTER MAXIMUM REPETITION RATE	0.5 Hz

ABB FTIR – FTLA2000 Analyzer

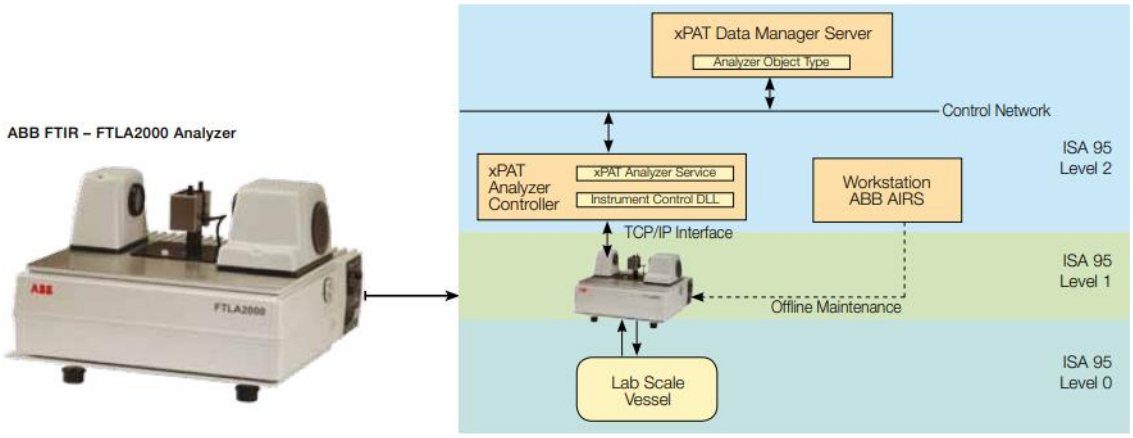

ABB FTIR SPECIFICATIONS

ANALYZER CLASS	IR spectrometer: FTLA2000-100 and FTLA2000-104				
	NIR spectrometer: FTLA2000-154 and FTLA2000-160				
SUBCLASS	Fourier Transform Spectrometer				
INTERFACE	Ethernet TCP/IP				
THROUGHPUT	Mid IR models			Near IR models	
	Resolution	Spectrum size	Max samples	Spectrum size	Max samples
	1 cm^{-1}	16384	Every 32 secs	32768	Every 64 secs
	2 cm^{-1}	8192	Every 16 secs	16384	Every 32 secs
	4 cm^{-1}	4096	Every 8 secs	8192	Every 16 secs
	8 cm^{-1}	2048	Every 5 secs	4096	Every 8 secs
	16 cm^{-1}	1024	Every 5 secs	2048	Every 5 secs
	32 cm^{-1}	512	Every 5 secs	1024	Every 5 secs
	64 cm^{-1}	256	Every 5 secs	512	Every 5 secs
	128 cm^{-1}	128	Every 5 secs	256	Every 5 secs

APPENDIX B

Ray-tracing Model

The main assumption of the Discrete Transfer Radiation Model (DTRM) is that the radiation leaving the surface element in a certain range of solid angles can be approximated by a single ray. This section provides details about the equations used in the DTRM.

The equation for the change of radiant intensity, dI, along a path, ds, can be written as:

$$\frac{dI}{ds} + aI = \frac{a\sigma T^4}{\pi} \tag{A.1}$$

where a is gas absorption coefficient, I is intensity, T is gas local temperature, and σ is Stefan-Boltzmann constant. Here, the refractive index is assumed to be unity. The DTRM integrates the above equation along a series of rays emanating from boundary faces. If a is constant along the ray, then $I(s)$ can be estimated as:

$$I(s) = \frac{\sigma T^4}{\pi}(1 - e^{-as}) + I_0 e^{-as} \tag{A.2}$$

where I_0 is the radiant intensity at the start of the incremental path, which is determined by the appropriate boundary condition. The energy source in the fluid due to radiation is then computed by summing the change in intensity along the path of each ray that is traced through the fluid control volume. The ray-tracing technique used in the DTRM can

provide a prediction of radiative heat transfer between surfaces without explicit view factor calculations.

In the ray-tracing method, the ray paths are calculated and stored prior to the fluid flow calculation. At each radiating face, rays are fired at discrete values of the polar and azimuthal angles (see Figure below). To cover the radiating hemisphere, θ is varied from 0 to $\pi/2$ and Φ from 0 to 2π. Each ray is then traced to determine the control volumes it intercepts as well as its length within each control volume. This information is then stored in the radiation file, which must be read in before the fluid flow calculations begin.

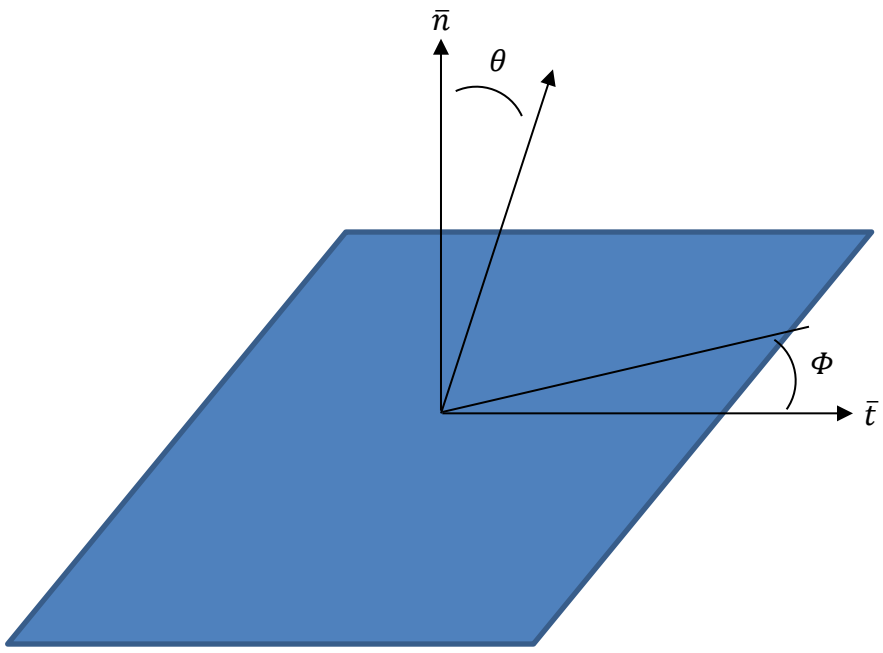

RNG K-ε Model

Multiphase turbulence modeling typically involves two equation models that are based on single-phase models and often cannot accurately capture the underlying flow physics. Additional turbulence modeling for multiphase flows is diminished even more when the basic underlying single-phase model cannot capture the complex physics of the flow. In such situations, the logical next step is to combine the Reynolds stress model (RSM) with the multiphase algorithm in order to handle challenging situations in which both factors, RSM for turbulence and the Eulerian multiphase formulation, are a precondition for accurate predictions.

The phase-averaged continuity and momentum equations for a continuous phase are:

$$\frac{\partial}{\partial t}(\overline{\alpha_c}\rho_c) + \nabla \cdot \left(\overline{\alpha_c}\rho_c \widetilde{U}_c\right) = 0 \tag{B.1}$$

$$\frac{\partial}{\partial t}\left(\overline{\alpha_c}\rho_{rmc}\widetilde{U}_c\right) + \nabla \cdot \left(\overline{\alpha_c}\rho_{rmc}\widetilde{U}_c \otimes \widetilde{U}_c\right) = -\overline{\alpha_c}\nabla\tilde{p} + \nabla \cdot \widetilde{\tau_c}^{\,t} + F_{Dc} \tag{B.2}$$

For simplicity, the laminar stress-strain tensor and other body forces such as gravity have been omitted from Eq. (B.1) and (B.2). The tilde denotes phase-averaged variables while an overbar reflects time-averaged values. In general, any variable Φ can have a phase-average value defined as

$$\widetilde{\Phi}_c = \frac{\overline{\alpha_c \Phi_c}}{\overline{\alpha_c}} \tag{B.3}$$

Considering only two phases for simplicity, the drag force between the continuous and the dispersed phases can be defined as:

$$F_{Dc} = K_{dc}\left[\left(\widetilde{U}_d - \widetilde{U}_c\right) - \left(\frac{\overline{\alpha_d u_d'}}{\overline{\alpha_d}} - \frac{\overline{\alpha_c u_c'}}{\overline{\alpha_c}}\right)\right] \tag{B.4}$$

where K_{dc} is the drag coefficient. Several terms in the Eq. (B.4) need to be modeled in order to close the phase-averaged momentum equations. This section describes the different modeling definition of the turbulent stresses $\tau^{\tilde{t}}$ that appears in Eq. (B.2).

The turbulent stress that appears in the momentum equations need to be defined on a per-phase basis and can be calculated as:

$$\tau_k^{\tilde{t}} = -\overline{\alpha_k}\rho_k \tilde{R}_{k,ij} \tag{B.5}$$

where the subscript k is replaced by c for the primary phase or by d for any secondary phases. As is the case for single-phase flows, the current multiphase RSM also solves the transport equations for Reynolds stresses R_{ij}. ANSYS FLUENT includes two methods for modeling turbulence in multiphase flows within the context of the RSM model: the dispersed turbulence model, and the mixture turbulence model.

REFERENCES

[1] Dakcoled, “Recent Outdoor LED Display Market Trend,” DAKCO. Las Vegans, NV, USA. Mar. 13, 2019. [Online]. Available: https://www.dakcoled.com/blog/outdoor-led-display-market-trend.html

[2] J. J. Laity, “The Climatic Footwork,” in Deserts and Desert Environments, vol. 3, Hoboken, NJ, USA: John Wiley and Sons. John Wiley and Sons, ch. 3, sec. 1, pp. 48-50. 2009.

[3] L. Wald. “Basics in Solar Radiation at Earth Surface,” HAL Id: hal-01676634, MINES Paris Technology., PSL Research University, 2018.

[4] LG-MRI, “Sunlight and Solar Clearing with LCD Displays,” Manufacturing Resources International. Alpharetta, GA, USA. Oct. 19, 2016. [Online]. Available: http://lg-mri.com/sunlight-and-solar-clearing

[5] Heat exchanger for an electronic display, by W. Dun and T. Hubbard. (2015, August 25). U.S. Patent No. 9119325 [Online]. Available: U.S. Patent and Trademark Office. Washington D.C. https://patents.google.com/patent/US9119325?oq=U.S.+Patent+No.+9119325

[6] J. Kim, J. M. Brown, Y. Joshi, K. O’Connor and M. Diaz, “Thermal Modeling of Air Cooled Outdoor Digital Displays,” in IEEE Intersociety Thermal and Thermomechanical Phenomena in Electronic Systems, Las Vegas, NV, USA, 2019, pp. 391-398.

[7] G. Yoon, S. Bae, Y. Lee, J. Yoon, “Edge-lit LCD Backlight Unit for 2D Local Dimming,” in Optics Express 20802, vol. 26, no. 16. 2018.

[8] Y, Chen, “Micro LED & Mini LED Market Expects Explosive Business Opportunities, with an Estimated Market Value of $1.38 Billion by 2022,” LEDinside of TrendForce Corporation. Shenzen, China. Jun. 20, 2018. [Online] Availabe: https://www.ledinside.com/intelligence/2018/6/microled_miniled_market_expects_explosive_business_opportunities_with_an_estimated_market_value_of_1_38_billion_by_2022

[9] Sparton, “What Is Considered a True Sunlight Readable or Outdoor Readable LCD,” Sparton Rugged Electronics, Woodbridge, ON, Canada. Dec. 11, 2015. [Online]. Available: https://www.spartonre.com/faqs/considered-true-sunlight-readable-outdoor-readable-lcd

[10] M. Anandan, “Progress of LED backlights for LCDs,” in Journal of the Society for Information Display, 16: 287-310. doi:10.1889/1.2841864. 2018.

[11] Y. Joshi, J. M. Brown, “Thermal Management of Outdoor Digital Displays – A Review,” in IEEE Intersociety Thermal and Thermomechanical Phenomena in Electronic Systems, Las Vegas, NV, USA, 2019, pp. 772-779.

[12] C. Demers, “Local Dimming on TVs: Direct-lit, Edge-lit, Full-array,” Rtings, Montreal, Canada. Jun. 01, 2016. [Online] Available: https://www.rtings.com/tv/tests/picture-quality/local-dimming (Accessed July 20 2019)

[13] W. Luiten, Philips, “The Latest Phillips TVs Make LEDs Dance,” Mentor Graphics, Engineering Edge, vol. 2, issue 3. [Online]. Available: https://www.mentor.com/products/mechanical/engineering-edge/volume2/issue3/philips-tv-led

[14] R. S. West, H. Konijn, W. Sillevis-Smitt, S. Kuppens, N. Pfeffer, Y. Martynov, Y. Takaaki, S. Eberle, G. Harbers, T. W. Tan, C. E. Chan, “43.4: High Brightness Direct LED Backlight for LCD-TV,” in SID Symposium Digest of Technical Papers, 2003. 34: 1262-1265. doi:10.1889/1.1832516.

[15] D. Hsieh, “Direct LED Backlight Technology Reigns Supreme in TV Panels,” IHS Markit, London, UK. Jan. 17, 2018. [Online]. Available: https://ihsmarkit.com/research-analysis/direct-led-backlight-technology-reigns-supreme.html (Accessed 09 2019)

[16] B. Kim, J. Kim, W. S. Ohm, S. Kang, "Eliminating hotspots in a multi-chip LED array direct backlight system with optimal patterned reflectors for uniform illuminance and minimal system thickness," in Optics Express, 10.1364/OE.18.008595. pp. 8595-8604. 2010.

[17] Y. Wang, J. Cen, W. Cao, F. Jiang, “Thermal Performance of Direct Illumination High-power LED Backlight Units with Different Assembling Structures,” in Heat and Mass Transfer, 53: 10.1007/s00231-016-1925-z. pp. 1-12. 2017.

[18] W. Luiten, J. T. Weeme, “Thermal management of LED-LCD TV display,” in Journal of the Society for Information Display. 19. 10.1889/JSID19.12.931. pp. 931-942. 2011.

[19] M. Marongiu, “Thermal Management of Displays/Signage in Outdoor Enclosures,” Electronics Cooling Blog, Featured, LED/Lighting, Thermal Management. Apr. 10, 2019. [Online]. Available: https://www.electronics-cooling.com/2019/04/thermal-management-of-displays-signage-in-outdoor-enclosures/

[20] M. Marongiu, “Balancing Heat Load and Cost As Digital Displays Venture Outside,” Electronics Cooling Blog, Featured, LED/Lighting, Thermal Management. Sep. 16, 2015.

[21] B. Medvitz, “Challenges for Outdoor Digital Displays,” in Information Display, vol. 32, no. 3, pp. 38-42, May 2016.

[22] FT Exploring Science and Technology, “Direct, Diffuse and Reflected Radiation,” AM Watson and David E. Watson, 2011. [Online]. Available: http://www.ftexploring.com/solar-energy/direct-and-diffuse-radiation.htm

[23] S. Wilbert, T. Stoffel, D. Myers, S. Wilcox, A. Habte, F. Vignola, J. Wood and L. Martin Pomares. “Measuring Solar Radiation and Relevant Atmospheric Parameters,” in Best Practices Handbook for the Collection and Use of Solar Resource Data for Solar Energy Applications, 2nd ed. Golden, CO, USA. National Renewable Energy Laboratory. 2017.

[24] CUBIT, “Sculpt Adaptive Meshing,” Sandia National Laboratories, Roswell, GA, USA. [Online]. Available: https://cubit.sandia.gov/public/15.4/help_manual/WebHelp/mesh_generation/meshing_schemes/parallel/sculpt_adapt.htm

[25] C. Yan, J. Yu and J. Li. “Scheme Effect and Grid Dependency in CFD Computations of Heat Transfer,” ACTA Aerodynamica Sinica. 2006, 24(1): pp. 125-130.

[26] I. Mishey. “Nonconforming Finite Volume Methods,” in Computational Geosciences. September 2002, vol. 6, issue 3-4, pp. 253-268. https://doi.org/10.1023/A:1021214424953.

[27] P. Yang, C. Chen, Z. M. Zhang, “A Dual-Layer Structure with Record-High Solar Reflectance for Daytime Radiative Cooling,” in Solar Energy, vol. 169, pp. 316-324. Jul. 15, 2018.

[28] Q. Cheng, P. Yang, Z. M. Zhang, “Radiative Properties of Ceramic Al203, AIN and Si3N4: I. Experiments,” in International Journal of Thermophysics, vol. 37, issue 6, id: 62, pp. 16. Jun. 2016.

[29] F. P. Incropera, D. P. DeWitt, T. L. Bergman and A. S. Lavine. “Radiation: Processes and Properties,” in Fundamentals of Heat and Mass Transfer. 6th ed. USA: John Wiley and Sons, pp. 744-775. 2007.

[30] Z. M. Zhang, “Fundamentals of Thermal Radiation,” Nano and Microscale Heat Transfer, McGraw-Hill Companies, Inc, chapter 8, pp. 283-290. 2007.

[31] National Renewable Energy Laboratory, “Reference Air Mass 1.5 Spectra,” NREL, Golden, Colorado, USA. [Online]. Available: https://www.nrel.gov/grid/solarresource/spectra-am1.5.html (Accessed April 09

[32] J. Stein, M. M. Hydeman, “Development and Testing of the Characteristic Curve Fan Model,” in ASHRAE Transactions: Symposia, AN-04-3-1, pp. 347-356. 2004.

[33] N. Peterman, “Research Tool Dissemination to Increase Energy Efficient Fenestration Product Penetration,” Efficient Windows Collaborative, Final Technical Report prepared for the U.S. Department of Energy, DE-FC26-06NT42766. Feb. 28, 2010. [Online]. Available: https://www.osti.gov/servlets/purl/1024896